Computer Methods in Applied Mechanics and Engineering 441 (2025) 117996

Contents lists available at ScienceDirect

Comput. Methods Appl. Mech. Engrg.

journal homepage: www.elsevier.com/locate/cma

A staggered grid shell particle method for shell structural damage subjected to underwater explosion☆

Jiasheng Li [a], Yong Liang [b], Zhixin Zeng [a], Xiong Zhang [a,*]

[a] School of Aerospace Engineering, Tsinghua University, Beijing 100084, PR China
[b] State Key Laboratory for Strength and Vibration of Mechanical Structures, School of Aerospace Engineering, Xi'an Jiaotong University, Xi'an 710049, PR China

ARTICLE INFO

Keywords:
Material point method
Solid shell
Staggered grid
Structural damage
Underwater explosion

ABSTRACT

A novel staggered grid shell particle method (SGSPM) is proposed in this paper to model the shell structural damage subjected to underwater explosion. The material point method (MPM) is used to model the fluid in underwater explosion, and the solid shell material point method (SSMPM) is adopted to model the shell structures. A staggered grid scheme is employed to eliminate the cell crossing noise and improve the accuracy of fluid simulation, and a conversion algorithm is proposed to handle the dynamic fracture of shell structures. In addition, a local multi-mesh contact method is introduced into the staggered grid scheme for modeling the fluid–structure interaction. Several numerical examples, including full hemispherical shell, penetration of a thin plate, large deformation of a plate subjected to underwater explosion, fragmentation of a plate and structural damage of a ship hull subjected to contact underwater explosion, are studied by the proposed SGSPM, and the numerical results agree well with the data in the literature and experiments.

1. Introduction

Underwater explosion is a class of extreme deformation problems and always causes severe damage to ship shell structures in engineering practice. To guide the design of engineering structures, the structural damage subjected to underwater explosion has attracted great attention. Experimental research and numerical research are important methods for evaluating the damage of ship structures. However, the cost of damage experiments on large engineering structures is extremely high. Therefore, the development of efficient and powerful numerical methods to simulate structural damage subjected to underwater explosion remains an active field of research.

Dynamic fracture of shell structures and multi-phase flow in underwater explosion are two challenges in this numerical study. Dynamic fracture involves extreme deformation and fragmentation. Traditional mesh-based methods suffer from mesh distortion and violate the law of mass conservation with erosion algorithms. Mesh-free methods, such as the material point method (MPM) [1,2], smoothed particle hydrodynamics (SPH) [3,4], element-free Galerkin (EFG) method [5–8], reproducing kernel particle method (RKPM) [9–12] and peridynamics (PD) [13–15] have been found to be more suitable for simulating dynamic fracture. Maurel and Combescure [4] presented a SPH shell formulation suitable for the simulation of shell fracture under impact. Peng et al. introduced a shell formulation in RKPM for the large deformation of curved shells [11] and further proposed a crack propagation algorithm for dynamic fracture in shell structures [12]. Behzadinasaba et al. [14] introduced a Kirchhoff–Love shell formulation in PD for modeling

☆ Supported by the National Natural Science Foundation of China with Grant Number 12472204.
* Corresponding author.
E-mail address: xzhang@tsinghua.edu.cn (X. Zhang).

https://doi.org/10.1016/j.cma.2025.117996
Received 2 January 2025; Received in revised form 13 March 2025; Accepted 3 April 2025
Available online 16 April 2025
0045-7825/© 2025 Elsevier B.V. All rights are reserved, including those for text and data mining, AI training, and similar technologies.

large elasto-plastic deformations and fracture of shell structures. It is attractive that these methods combine the high efficiency of shell formulation with the advantages of mesh-free methods in dynamic fracture. The multi-phase flow in underwater explosion involves moving material interfaces of the gas, liquid and solid. Traditional mesh-based methods require an additional technique to capture the multi-phase interface, such as volume of fluid method [16] and level-set method [17]. Mesh-free methods discretize the domain with Lagrangian particles, so that the interfaces can be automatically tracked and the algorithm complexity can be reduced. Liu et al. [18] used the SPH to simulate the underwater explosion. Peng et al. [19] proposed a numerical model by coupling the SPH and RKPM shell formulation to simulate structural damage subjected to underwater explosion. Therefore, mesh-free methods have remarkable capabilities in modeling structural damage subjected to underwater explosion.

The material point method (MPM) is a typical representative of mesh-free methods. The MPM adopts a set of Lagrangian particles moving through an Eulerian background grid to surmount the challenges in simulations of extreme deformation. The MPM has shown its success in simulating various kinds of extreme deformation events during these decades, such as hyper velocity impact [20–23], penetration [24,25], fracture evolution [26–32], fluid flow [33–37] and fluid–structure interaction [38–42]. Many variants have been proposed to improve the accuracy and stability of MPM [43–53]. Bardenhagen et al. [43] developed the generalized interpolation material point (GIMP) method by accounting for spatial volume of each particle to reduce the cell crossing noise caused by the discontinuity in the gradient of linear shape function. Liang et al. [50,54] proposed the staggered grid material point (SGMP) method with the volume integrals in the weak form evaluated by cell center quadrature instead of particle quadrature to eliminate the cell crossing noise. Some variants have been presented for shell formulation in MPM [55,56]. Guo et al. [55] combined MPM and subdivision finite elements for thin-shell simulations with frictional contact. Li et al. [56] developed the solid shell material point method (SSMPM) with shell particles and locking treatments for the large deformation of shell structures. However, few work of MPM has explored the area of structural damage subjected to underwater explosion.

The MPM has been used to simulate the dynamic fracture of shell structures without underwater explosion. Yang et al. [57] used the MPM to simulate the fragmentation of a cylinder shell and a sphere shell driven by air explosion. Zhang et al. [58] proposed an explicit phase-field total Lagrangian material point method to model the collision and fracture of two hollow cylinder shells. To avoid locking phenomena in coarse background grid, the discretization size of background grid in their simulations was less than 1/5 of the shell thickness, which would lead to prohibitive computational cost. On the contrary, it is inspiring that shell formulation can surmount the numerical difficulties and achieve high efficiency. However, dynamic fracture simulation is difficult for the shell formulation of Guo et al. [55], because finite elements with rotational degrees of freedom (DOFs) are used to discrete shell structures. To solve this problem, the SSMPM is developed and considered to be more suitable for handling dynamic fracture of shell structures, although a conversion scheme to automatically simulate fracture is still required [56]. For the structural damage subjected to underwater explosion, the computational scale of simulation model is usually huge. The cell crossing noise would affect the solution accuracy if using the MPM to simulate the multi-phase flow in underwater explosion. Therefore, there is no suitable numerical method in the framework of MPM for the structural damage subjected to underwater explosion, which is the main target of this work.

In the present work, a novel staggered grid shell particle method (SGSPM) is developed by introducing the staggered grid scheme and conversion algorithm into the SSMPM and employing a local multi-mesh contact method. The fluid in underwater explosion is discretized by MPM particles. The cell center quadrature is employed with the staggered grid scheme to eliminate the cell crossing noise and to improve the accuracy of fluid simulation. The shell structures are discretized by shell particles. To be consistent with the scheme of fluid, the shell particles are also updated through the staggered grid scheme. For the dynamic fracture of shell structures, a conversion algorithm is employed to adaptively convert shell particles into MPM particles. And then, the MPM particles can be used to easily describe fracture. Moreover, the shell particles and MPM particles have only displacement DOFs and are updated by the staggered grid. Without additional algorithms, they can be naturally coupled for the interaction between the remaining shell particles and converted MPM particles. The advantages of the shell particles to simulate bending deformation and the MPM particles to simulate fragmentation are combined. A local multi-mesh contact method is proposed in the staggered grid scheme for the interaction between the fluid and shell structures. Several numerical examples, including hemispherical shell, penetration of a thin plate by a ball and extreme deformation of shell structures subjected to underwater explosion, are studied to verify and validate the proposed method, and numerical results are in good agreement with the data in the literature and experiments.

The rest of this paper is organized as follows. In Section 2, the basic idea of SSMPM and its shortcomings in the simulation of structural damage subjected to underwater explosion are briefly reviewed. Then, Section 3 presents the detailed methodology of the proposed SGSPM in terms of the staggered grid scheme and conversion algorithm. And a local multi-mesh contact method for the fluid–structure interaction is presented in Section 4. The algorithm summary and remark of the SGSPM are given in Section 5. Validations and benchmark simulations are presented in Section 6. Finally Section 7 gives the conclusion.

2. Brief review of the solid shell material point method

The weak form equivalent to momentum equations and traction boundary condition in updated Lagrangian formulation is given as

$$\int_{\Omega} \rho \ddot{\boldsymbol{u}} \cdot \delta \boldsymbol{u} \mathrm{d}V + \int_{\Omega} \boldsymbol{\sigma} : \delta \boldsymbol{\varepsilon} \mathrm{d}V - \int_{\Omega} \rho \boldsymbol{b} \cdot \delta \boldsymbol{u} \mathrm{d}V - \int_{\Gamma_t} \bar{\boldsymbol{t}} \cdot \delta \boldsymbol{u} \mathrm{d}A = 0 \tag{1}$$

where Γ_t denotes the traction boundary of material domain Ω, ρ is the current density, $\boldsymbol{u}$ is the displacement, $\delta \boldsymbol{u}$ is the virtual displacement, $\boldsymbol{\sigma}$ is the Cauchy stress in the current configuration, $\boldsymbol{\varepsilon}$ is the Cauchy strain, $\boldsymbol{b}$ is the body force per unit mass and $\bar{\boldsymbol{t}}$ is the traction on the boundary.

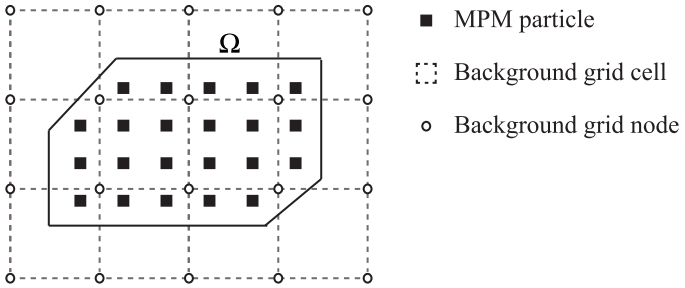


Fig. 1. Spatial discretization of extremely deformed objects by MPM particles.

The SSMPM [56] adopts Lagrangian particles and an Eulerian background grid for spatial discretization. The MPM particles are used for extremely deformed objects, and the shell particles are adopted for shell structures. The background grid is used to integrate momentum equations. The SSMPM adopts leapfrog central difference integration scheme for temporal discretization. Same as the standard MPM, the computational process of the SSMPM in each time step consists of four steps: (1) particle-to-grid projection, (2) background grid momentum updating, (3) grid-to-particle mapping and particle updating, and (4) resetting the background grid.

2.1. Spatial discretization

2.1.1. MPM particle

In the MPM, the material domain Ω of extremely deformed objects is discretized into a set of MPM particles, as illustrated in Fig. 1. The MPM particles act as quadrature points in calculating the integration of weak form equation. The density can be given by

$$\rho(\boldsymbol{x}) = \sum_{p=1}^{n_\mathrm{p}} m_p \delta(\boldsymbol{x} - \boldsymbol{x}_p) \tag{2}$$

where the subscript p denotes the variables associated with particle p, n_p is the total number of particles, m_p is the mass of particle p, δ is the Dirac delta function with dimension of the inverse of particle volume, $\boldsymbol{x}$ is the spatial coordinates in the current configuration, and $\boldsymbol{x}_p$ is the coordinates of particle p.

The displacement field $\boldsymbol{u}(\boldsymbol{x})$ of the computational domain is interpolated from the grid nodal displacement $\boldsymbol{u}_I$ by the shape function $N_I(\boldsymbol{x})$ of each grid node I, namely

$$\boldsymbol{u}(\boldsymbol{x}) = \sum_{I=1}^{n_\mathrm{g}} N_I(\boldsymbol{x}) \boldsymbol{u}_I \tag{3}$$

where the subscript I denotes the variables associated with the grid node I, n_g is the total number of background grid nodes, $N_I(\boldsymbol{x})$ is the shape function.

Substituting Eqs. (2) and (3) into the weak form Eq. (1) and invoking the arbitrariness of the virtual displacement $\delta \boldsymbol{u}_I$ lead to the discretized momentum equations at each grid node

$$\dot{\boldsymbol{p}}_I = \boldsymbol{f}_I^{\mathrm{int}} + \boldsymbol{f}_I^{\mathrm{ext}}, \quad \forall \boldsymbol{x}_I \notin \Gamma_u \tag{4}$$

in which Γ_u is the displacement boundary of the material domain,

$$\boldsymbol{p}_I = m_I \dot{\boldsymbol{u}}_I \tag{5}$$

is the momentum at grid node I,

$$m_I = \sum_{p=1}^{n_\mathrm{p}} m_p N_I(\boldsymbol{x}_p) \tag{6}$$

is the lumped grid mass matrix,

$$\boldsymbol{f}_I^{\mathrm{int}} = -\sum_{p=1}^{n_\mathrm{p}} \nabla N_{Ip} \cdot \boldsymbol{\sigma}_p V_p \tag{7}$$

and

$$\boldsymbol{f}_I^{\mathrm{ext}} = \sum_{p=1}^{n_\mathrm{p}} m_p N_{Ip} \boldsymbol{b}_p + \sum_{p=1}^{n_\mathrm{p}} N_{Ip} \bar{\boldsymbol{t}}_p h^{-1} V_p \tag{8}$$

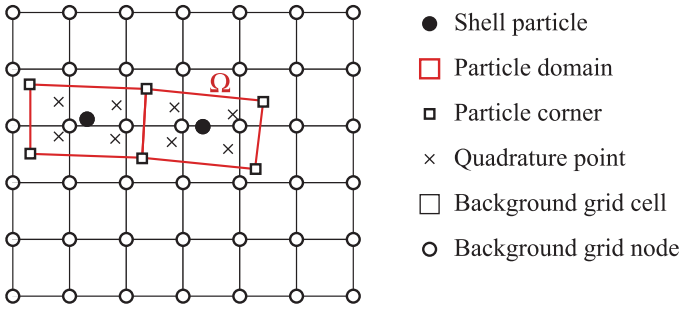


Fig. 2. Spatial discretization of shell structures by shell particles.

are the internal and external nodal forces, respectively. In Eq. (7), $N_{Ip} = N_I(\boldsymbol{x}_p)$ is the shape function of node I evaluated at the position of particle p, $\boldsymbol{\sigma}_p$ is the stress of particle p and V_p is the volume of particle p. In Eq. (8), $\boldsymbol{b}_p$ is the body force per unit mass of particle p, $\bar{\boldsymbol{t}}_p$ is the traction of particle p and h is the thickness of the fictitious layer used to convert the surface integral into a volume integral. Here, the strain rate $\dot{\boldsymbol{\varepsilon}}_p$ and vorticity rate $\dot{\boldsymbol{\Omega}}_p$ for calculating $\boldsymbol{\sigma}_p$ are given as

$$\dot{\boldsymbol{\varepsilon}}_p = \sum_{I=1}^{n_g} \frac{1}{2} \left(\boldsymbol{v}_I \otimes \nabla N_{Ip} + \nabla N_{Ip} \otimes \boldsymbol{v}_I \right) \tag{9}$$

$$\dot{\boldsymbol{\Omega}}_p = \sum_{I=1}^{n_g} \frac{1}{2} \left(\boldsymbol{v}_I \otimes \nabla N_{Ip} - \nabla N_{Ip} \otimes \boldsymbol{v}_I \right) \tag{10}$$

where $\boldsymbol{v}_I$ is the grid nodal velocity.

The stress is updated by

$$\sigma_{ij}^{n+1} = \sigma_{ij}^{n} + \dot{\sigma}_{ij}^{n+1/2} \Delta t^{n+1/2} \tag{11}$$

where $\dot{\sigma}_{ij}^{n+1/2}$ is the stress rate at time $t^{n+1/2}$, σ_{ij}^{n+1} and σ_{ij}^{n} are the stress at times t^{n+1} and t^n, respectively. The leapfrog central difference integration scheme [59] is employed, and its details are provided in Section 2.2.

In order to correctly update the stress under finite deformation, the Jaumann rate [2]

$$\sigma_{ij}^{\nabla} = \dot{\sigma}_{ij} - \sigma_{im}\Omega_{jm} - \sigma_{mj}\Omega_{im} \tag{12}$$

is employed in the constitutive model to eliminate the effects of rigid body rotation. Here, $\Omega_{jm} = \dot{\Omega}_{jm}\Delta t$. Then, the stress is updated by

$$\sigma_{ij}^{n+1} = \sigma_{ij}^{n} + \left(\sigma_{im}^{n}\Omega_{jm}^{n+1/2} + \sigma_{mj}^{n}\Omega_{im}^{n+1/2} \right) \Delta t^{n+1/2} + \sigma_{ij}^{\nabla n+1/2} \Delta t^{n+1/2} \tag{13}$$

Although elastic–plastic constitutive laws are used in the examples in Section 6, the elastic constitutive model is introduced here to simplify the explanation of the stress update. In the elastic constitutive model,

$$\sigma_{ij}^{\nabla n+1/2} = C_{ijkl} \dot{\varepsilon}_{kl}^{n+1/2} \tag{14}$$

where C_{ijkl} is the elastic tensor.

2.1.2. Shell particle

In the SSMPM, the material domain Ω of shell structures is discretized into a single layer of shell particles, as illustrated in Fig. 2. The shell particles are defined by incorporating the concept of FEM within the MPM framework. A 3D shell particle consists of a hexahedral particle domain, eight particle corners and eight Gauss quadrature points. The particle domain is used to describe the geometry of the material domain. Quadrature points are employed to store historical variables, such as strain and stress. Mass, velocity, position and forces are calculated at particle corners. Particle corners have only displacement DOFs. The positions of the particle corners are also updated after integrating momentum equations on the background grid nodes to track the geometry of shell particles. Therefore, the coupling between shell particles and MPM particles is readily.

To integrate the discretized momentum equations at each grid node as Eq. (4), the lumped grid mass matrix from shell particles is given by

$$m_I = \sum_{c=1}^{n_c} N_{Ic} m_c \tag{15}$$

where

$$m_c = \sum_{p=1}^{n_p} \sum_{q=1}^{n_q} S_{cq}^{p} \rho V_q^p \tag{16}$$

is the mass of particle corner c. Here, the subscript c denotes the variables associated with particle corner c, n_c is the total number of particle corners, $S_{cq}^p = S_c^p(\boldsymbol{\xi}_q)$ is the shape function related to the cth corner of shell particle p evaluated at the qth quadrature point, V_q^p is the volume at the qth quadrature point of shell particle p and n_q is the number of quadrature points in a shell particle. The internal nodal force from shell particles is

$$\boldsymbol{f}_I^{\text{int}} = \sum_{c=1}^{n_c} N_{Ic} \boldsymbol{f}_c^{\text{int}} \tag{17}$$

where

$$\boldsymbol{f}_c^{\text{int}} = -\sum_{p=1}^{n_p} \sum_{q=1}^{n_q} \nabla S_{cq}^p \cdot \boldsymbol{\sigma}_q^p V_q^p \tag{18}$$

is the internal force of particle corner c, and $\boldsymbol{\sigma}_q^p$ is the stress at the qth quadrature point of shell particle p. The external nodal force from shell particles is

$$\boldsymbol{f}_I^{\text{ext}} = \sum_{c=1}^{n_c} N_{Ic} \boldsymbol{f}_c^{\text{ext}} \tag{19}$$

where

$$\boldsymbol{f}_c^{\text{ext}} = \sum_{p=1}^{n_p} \sum_{q=1}^{n_q} S_{cq}^p \rho \boldsymbol{b}_q^p V_q^p \tag{20}$$

is the external force of particle corner c with the traction term omitted for simplicity, and $\boldsymbol{b}_q^p$ is the body force per unit mass of particle p at its qth quadrature point. Here, the strain rate and vorticity rate for calculating $\boldsymbol{\sigma}_q^p$ are given as

$$\dot{\boldsymbol{\varepsilon}}_q^p = \sum_{c=1}^{n_c} \frac{1}{2} \left(\boldsymbol{v}_c \otimes \nabla S_{cq}^p + \nabla S_{cq}^p \otimes \boldsymbol{v}_c \right) \tag{21}$$

$$\dot{\boldsymbol{\Omega}}_q^p = \sum_{c=1}^{n_c} \frac{1}{2} \left(\boldsymbol{v}_c \otimes \nabla S_{cq}^p - \nabla S_{cq}^p \otimes \boldsymbol{v}_c \right) \tag{22}$$

where $\boldsymbol{v}_c$ is the velocity of particle corner c, $\dot{\boldsymbol{\varepsilon}}_q^p$ and $\dot{\boldsymbol{\Omega}}_q^p$ are the strain rate and vorticity rate at the qth quadrature point of shell particle p respectively. When the stress is updated, the volume and density of quadrature points are also updated. The volume is updated using Gauss quadrature

$$V_q^p = \sum_{k=1}^{2} \sum_{l=1}^{2} \sum_{m=1}^{2} w_k w_l w_m \left| \boldsymbol{J}(\xi_k, \eta_k, \zeta_k) \right| \tag{23}$$

where w_k, w_l and w_m are the weights at Gauss quadrature points; ξ_k, η_k and ζ_k are the natural coordinates of the Gauss quadrature points; and $\left| \boldsymbol{J}(\xi_k, \eta_k, \zeta_k) \right|$ is the determinant of the Jacobian matrix at quadrature points. The density of the quadrature points at time t^n is updated by

$$\rho_q^{p,n} = \frac{\rho_q^{p,0} V_q^{p,0}}{V_q^{p,n}} \tag{24}$$

where $V_q^{p,n}$ is the volume at the qth quadrature point of shell particle p at time t^n, and $\rho_q^{p,0}$ and $V_q^{p,0}$ are the density and volume of the quadrature point at the initial time $t^0 = 0$s.

The above formulation for shell particles is not sufficient to correctly simulate the bending deformation of shell structures. Shear locking, trapezoidal locking and thickness locking would cause an over stiff behavior of shell structures.

The assumed natural strain (ANS) method is introduced in shell particles to eliminate the shear locking and trapezoidal locking. In the natural coordinate system of the shell particle, as shown in Fig. 3, $\varepsilon_{\zeta\zeta}$ is accurate at sampling points S_1, S_2, S_3, S_4; $\varepsilon_{\eta\zeta}$ is accurate at sampling points S_5, S_6, S_7, S_8; and $\varepsilon_{\zeta\xi}$ is accurate at sampling points $S_9, S_{10}, S_{11}, S_{12}$. The respective strain components are first evaluated at the sampling points and then interpolated to calculate their values at the quadrature points.

The enhanced assumed strain (EAS) method is applied to shell particles for eliminating the thickness locking. The enhanced degrees of freedom, $\boldsymbol{\alpha}$, are defined at the particle centroid. The enhanced assumed strain field, $\bar{\boldsymbol{\varepsilon}}_e$, is calculated by

$$\bar{\boldsymbol{\varepsilon}}_e = \bar{\boldsymbol{B}}_e \boldsymbol{\alpha} \tag{25}$$

where $\bar{\boldsymbol{B}}_e$ is the enhanced assumed strain operator. The enhanced assumed strain field is then added to the original strain field to eliminate thickness locking. The details of the ANS and EAS methods can be found in the work of Li et al. [56].

Shell particles are inspired by the solid shell element in FEM. Based on the solid element in FEM, the ANS and EAS methods are introduced to correct strain and stress. As a result, the three-dimensional constitutive model can be directly adopted without modification. Therefore, the constitutive model and Jaumann rate used by the shell particles to update stress are the same as those of the MPM particles, as described at the end of Section 2.1.1.

With the precise description of bending deformation by the shell particles, a single layer of shell particles and a coarse background grid could be used in shell structure simulations. A coarse grid means that the shell particles occupy only one

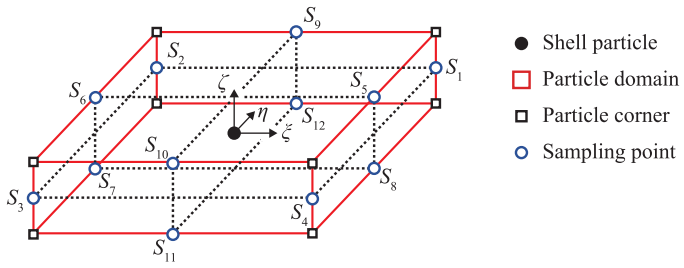


Fig. 3. The shell particle in the natural coordinate system [56].

or two layers of background grid cells in the thickness direction. Unlike the SSMPM, when using the MPM to simulate shell structures, the discretization size of background grid is typically smaller than 1/5 of the shell thickness, which results in prohibitive computational cost. The computational efficiency of shell simulations is significantly improved by the SSMPM compared to the MPM, as demonstrated in the work of Li et al. [56].

2.2. Temporal discretization

The leapfrog central difference integration scheme [59] is used in the SSMPM. In the step (2), the velocity $\boldsymbol{v}_I^{n+1/2}$ at time $t^{n+1/2}$ and the displacement $\boldsymbol{u}_I^{n+1}$ at time t^{n+1} are updated by

$$\boldsymbol{v}_I^{n+1/2} = \boldsymbol{v}_I^{n-1/2} + \boldsymbol{a}_I^n \Delta t^n \tag{26}$$

$$\boldsymbol{u}_I^{n+1} = \boldsymbol{u}_I^n + \boldsymbol{v}_I^{n+1/2} \Delta t^{n+1/2} \tag{27}$$

where

$$\Delta t^n = \frac{1}{2}(\Delta t^{n-1/2} + \Delta t^{n+1/2}) \tag{28}$$

is the time step at time t^n and $\Delta t^{n+1/2} = t^{n+1} - t^n$, and $\boldsymbol{a}_I^n$ is the acceleration at time t^n calculated by Eq. (4). For the stability requirement of central difference method, the critical time step is given as

$$\Delta t_{\mathrm{cr}} = \min\left[\frac{d_{\mathrm{g}}}{\max\limits_p\left(c_p + \left|\boldsymbol{v}_p\right|\right)}, \frac{d_{\mathrm{g}}}{\max\limits_{p,q}\left(c_q^p\right)}\right] \tag{29}$$

where d_{g} is the grid cell size, c_p is the sound speed of MPM particle p, $\boldsymbol{v}_p$ is the velocity of MPM particle p, and c_q^p is the sound speed at the qth quadrature point of shell particle p. The time step is taken as

$$\Delta t = \alpha \Delta t_{\mathrm{cr}} \tag{30}$$

where α is a constant that ranges from 0.6 to 0.8 in this work.

After momentum is updated on the background grid, the particle variables are updated by grid-to-particle mapping in the step (3). The MPM particles are updated by

$$\boldsymbol{v}_p^{n+1/2} = \boldsymbol{v}_p^{n-1/2} + \sum_{I=1}^{n_{\mathrm{g}}} N_{Ip} \boldsymbol{a}_I^n \Delta t^n \tag{31}$$

$$\boldsymbol{x}_p^{n+1} = \boldsymbol{x}_p^n + \sum_{I=1}^{n_{\mathrm{g}}} N_{Ip} \boldsymbol{v}_I^{n+1/2} \Delta t^{n+1/2} \tag{32}$$

The shell particle corners are updated by

$$\boldsymbol{v}_c^{n+1/2} = \boldsymbol{v}_c^{n-1/2} + \sum_{I=1}^{n_{\mathrm{g}}} N_{Ic} \boldsymbol{a}_I^n \Delta t^n \tag{33}$$

$$\boldsymbol{x}_c^{n+1} = \boldsymbol{x}_c^n + \sum_{I=1}^{n_{\mathrm{g}}} N_{Ic} \boldsymbol{v}_I^{n+1/2} \Delta t^{n+1/2} \tag{34}$$

so that the geometry of shell particles can be tracked.

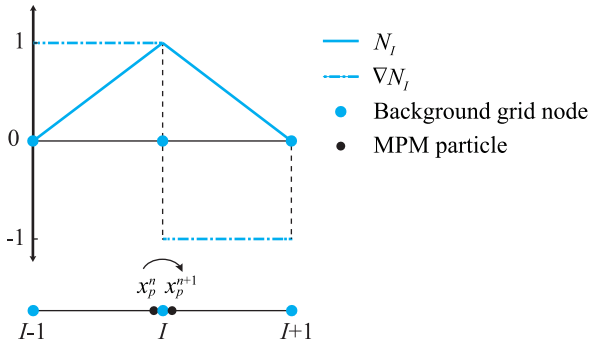


Fig. 4. Diagram of the cell crossing noise.

2.3. Shortcomings of the SSMPM in structural damage subjected to underwater explosion

The SSMPM suffers from the cell crossing noise and disability to automatically simulate dynamic fracture when modeling structural damage subjected to underwater explosion. Simulation accuracy is affected by the cell crossing noise. In the step (4) of the computational process, the MPM particles and shell particle corners may cross from a grid cell to another. Taking one dimension for example, the shape function of node I is given by

$$N_I(\xi) = \frac{1}{2}(1 + \xi\xi_I) \tag{35}$$

where ξ is the natural coordinate and ξ_I is the natural coordinate of node I. The shape function is continuous in the adjacent cells of node I, but the gradient of shape function is discontinuous between the adjacent cells, as illustrated in Fig. 4. Eqs. (17) and (18) for the internal nodal force from shell particles only involve the shape function, but Eq. (7) for the internal nodal force from MPM particles includes the gradient of shape function. Therefore, when the MPM particles crossing grid cell boundary, the internal nodal force would have a non-physical jump. This is called cell crossing noise and affects the accuracy of fluid simulation in underwater explosion.

The shell particles are able to describe bending deformation, but lack of the capacity for simulating dynamic fracture. The MPM particles can easily model fracture, but have difficulty simulating bending deformation. Neither shell particles nor MPM particles can be used alone to handle the dynamic fracture of shell structures. These two types of particles need to be combined by an additional algorithm, which will be further discussed in Section 3.2.

3. Staggered grid shell particle method

In this work, to simulate structural damage subjected to underwater explosion, a novel staggered grid shell particle method (SGSPM) is proposed by introducing the staggered grid scheme and conversion algorithm into the solid shell material point method. In Section 3.1, the staggered grid scheme is presented. In order to eliminate the cell crossing noise, the cell center quadrature is employed in calculating the mass, momentum and forces at grid nodes. The contribution of both MPM particles and shell particles are considered in the reconstruction of the physical quantities at cell centers. With the conversion algorithm in Section 3.2, shell particles under extreme deformation are adaptively converted into MPM particles and dynamic fracture could be simulated. The remaining shell particles and converted MPM particles are naturally coupled by the staggered grid. In the SGSPM, the leapfrog central difference integration scheme and the determination of time step are the same as those described in Section 2.2.

3.1. Staggered grid scheme

The staggered grid scheme is established in the framework of SSMPM. The computational process of the SGSPM in each time step is the same as that of SSMPM: (1) particle-to-grid projection, (2) background grid momentum updating, (3) grid-to-particle mapping and particle updating, and (4) resetting the background grid. However, key changes are introduced in the step (1) and step (3).

An auxiliary grid is generated by shifting the background grid by half the side length of its cells in each direction, as illustrated in Fig. 5. Consequently, the auxiliary grid nodes correspond to the cell centers of the background grid. The auxiliary grid and background grid together form the staggered grid. As shown in Fig. 5, the auxiliary grid can be divided into two regions: a single-layer boundary region (highlighted in blue) and an inner region (highlighted in yellow). In the inner region, each auxiliary grid node coincides with the cell center of the background grid. In the boundary region Ω_b, the shape function of auxiliary grid nodes, $N_a(\boldsymbol{x})$, must be corrected to satisfy the partition of unity. Take one-dimension as an example, the corrected shape function is defined as

$$N_a = \begin{cases} \frac{1}{2}\left(1 + \xi_a\xi\right) & \boldsymbol{x} \in \Omega - \Omega_b \\ 1 & \boldsymbol{x} \in \Omega_b \end{cases} \tag{36}$$

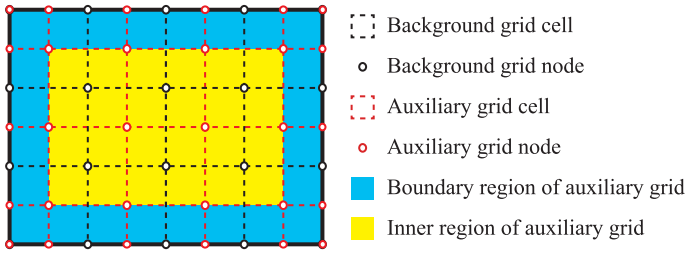


Fig. 5. The staggered grid consisting of an auxiliary grid and a background grid. (For interpretation of the references to color in this figure legend, the reader is referred to the web version of this article.)

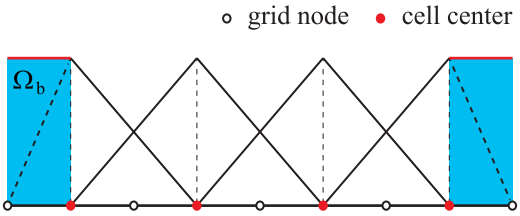


Fig. 6. The corrected shape function for the boundary cells of the auxiliary grid. (For interpretation of the references to color in this figure legend, the reader is referred to the web version of this article.)

which is illustrated in Fig. 6. In the boundary region Ω_b, the shape function is replaced by $N_a = 1$, as shown by the red line, while the rest remains unchanged. The three-dimensional shape function can be obtained by the tensor product of the three one-dimensional shape functions.

In the staggered grid, a rectangular background grid and a rectangular auxiliary grid are employed. Based on the coordinates $(x_{\min}, y_{\min}, z_{\min})$ and $(x_{\max}, y_{\max}, z_{\max})$, as well as the cell size d_g of the background grid, the relative positions and shape functions for both MPM particles and shell particle corners relative to the background grid and auxiliary grid can be obtained through simple and efficient calculations. Furthermore, the relative positions and shape functions remain unchanged during each time step, they only need to be calculated once at the beginning of each time step, resulting in low computational cost.

Structural damage subjected to underwater explosion consists of the flow in underwater explosion and dynamic fracture of shell structures. They are simulated by different types of particles.

3.1.1. Particles for fluid

The fluid in underwater explosion is simulated by MPM particles, as shown in Fig. 7. In the step (1), the physical quantities at grid nodes are evaluated by the cell center quadrature, namely,

$$m_I = \sum_{a=1}^{n_a} N_{Ia} m_a \tag{37}$$

$$\boldsymbol{p}_I = \sum_{a=1}^{n_a} N_{Ia} \boldsymbol{p}_a \tag{38}$$

$$\boldsymbol{f}_I^{\text{int}} = -\sum_{a=1}^{n_a} \nabla N_{Ia} \cdot \boldsymbol{\sigma}_a V_a \tag{39}$$

$$\boldsymbol{f}_I^{\text{ext}} = \sum_{a=1}^{n_a} N_{Ia} m_a \boldsymbol{b}_a \tag{40}$$

where the subscript a denotes the variables associated with cell center a, n_a is the total number of background grid cells, $N_{Ia} = N_I(\boldsymbol{x}_a)$ is the shape function of node I evaluated at the cell center $\boldsymbol{x}_a$, m_a is the cell mass and V_a is the cell volume. The 8-node trilinear hexahedron cell is used and N_{Ia} equals to $1/8$.

The quantities m_a, $\boldsymbol{p}_a$, $\boldsymbol{\sigma}_a V_a$ and $m_a \boldsymbol{b}_a$ at cell centers are reconstructed from MPM particles through the auxiliary grid, namely,

$$m_a = \sum_{p=1}^{n_p} N_{ap} m_p \tag{41}$$

$$\boldsymbol{p}_a = \sum_{p=1}^{n_p} N_{ap} m_p \boldsymbol{v}_p \tag{42}$$

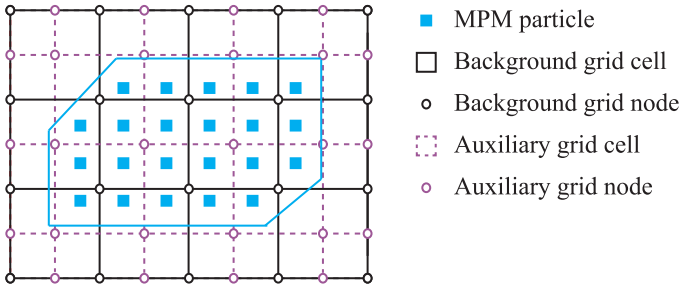


Fig. 7. MPM particles for fluid in the SGSPM.

$$\boldsymbol{\sigma}_a V_a = \sum_{p=1}^{n_\mathrm{p}} N_{ap} \boldsymbol{\sigma}_p V_p \tag{43}$$

$$m_a \boldsymbol{b}_a = \sum_{p=1}^{n_\mathrm{p}} N_{ap} m_p \boldsymbol{b}_p \tag{44}$$

where $N_{ap} = N_a(\boldsymbol{x}_p)$ is the shape function of auxiliary grid node a evaluated at the position of particle p (see Fig. 7).

The grid-to-particle mapping scheme in the step (3) is consistent with above mapping scheme. The physical quantities at cell centers are calculated from those at background grid nodes and then used to update the information of particles. The acceleration, velocity, strain rate and vorticity rate at cell centers are given as

$$\boldsymbol{a}_a = \sum_{I=1}^{8} N_{Ia} \boldsymbol{a}_I \tag{45}$$

$$\boldsymbol{v}_a = \sum_{I=1}^{8} N_{Ia} \boldsymbol{v}_I \tag{46}$$

$$\dot{\boldsymbol{\varepsilon}}_a = \sum_{I=1}^{n_\mathrm{g}} \frac{1}{2} \left(\boldsymbol{v}_I \otimes \nabla N_{Ia} + \nabla N_{Ia} \otimes \boldsymbol{v}_I \right) \tag{47}$$

$$\dot{\boldsymbol{\Omega}}_a = \sum_{I=1}^{n_\mathrm{g}} \frac{1}{2} \left(\boldsymbol{v}_I \otimes \nabla N_{Ia} - \nabla N_{Ia} \otimes \boldsymbol{v}_I \right) \tag{48}$$

The MPM particles are updated by

$$\boldsymbol{v}_p^{n+1/2} = \boldsymbol{v}_p^{n-1/2} + \sum_{a=1}^{n_\mathrm{a}} N_{ap} \boldsymbol{a}_a^n \Delta t^n \tag{49}$$

$$\boldsymbol{x}_p^{n+1} = \boldsymbol{x}_p^n + \sum_{a=1}^{n_\mathrm{a}} N_{ap} \boldsymbol{v}_a^{n+1/2} \Delta t^{n+1/2} \tag{50}$$

$$\dot{\boldsymbol{\varepsilon}}_p = \sum_{a=1}^{n_\mathrm{a}} N_{ap} \dot{\boldsymbol{\varepsilon}}_a \tag{51}$$

$$\dot{\boldsymbol{\Omega}}_p = \sum_{a=1}^{n_\mathrm{a}} N_{ap} \dot{\boldsymbol{\Omega}}_a \tag{52}$$

The auxiliary grid plays a key role in the mapping between MPM particles and background gird in the step (1) and step (3). And the cell crossing noise in the MPM particles for fluid is eliminated by the staggered grid scheme.

The fluid in underwater explosion consists of the explosive products of TNT, water and air. The air is ignored in the simulation because its effect on structural damage is negligible. The explosive products and water are modeled using MPM particles with different equations of state. In this work, spherical TNT is employed, and the detonation point is located at the center of the sphere. After the TNT is detonated, the pressure of the explosive products, p_{exp}, is determined by the JWL equation of state and burn fraction [2], namely

$$p_{\mathrm{exp}} = F p_{\mathrm{JWL}} \tag{53}$$

The burn fraction is

$$F = \begin{cases} \frac{(t - t_L) D}{1.5 d_\mathrm{g}} & t > t_L \\ 0 & t \le t_L \end{cases} \tag{54}$$

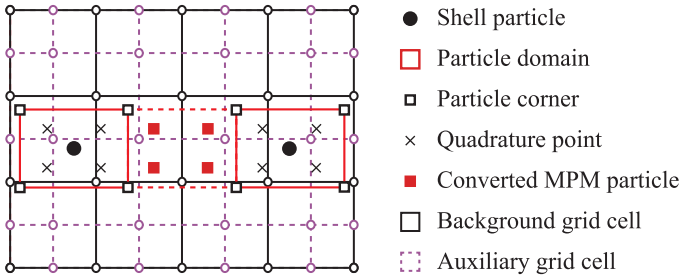


Fig. 8. Particles for shell structures in the SGSPM.

where t is current time, $t_L = 0$s is detonation time and $D = 6930$ m/s is detonation velocity. When the burn fraction $F > 1$, F is set to 1. The JWL equation of state is

$$p_{\mathrm{JWL}} = A\left(1 - \frac{\omega}{R_1 V}\right) e^{-R_1 V} + B\left(1 - \frac{\omega}{R_2 V}\right) e^{-R_2 V} + \omega\rho e \tag{55}$$

where $A = 3.712 \times 10^5$MPa, $B = 3.21 \times 10^3$MPa, $R_1 = 4.15$, $R_2 = 0.95$ and $\omega = 0.3$. $V = \rho_0/\rho$ is the relative volume. The initial density and the specific internal energy are $\rho_0 = 1630$ kg/m^3 and $e_0 = 4.29 \times 10^6$ J/kg, respectively.

The water is modeled by MPM particles with the Mie–Gruneisen equation of state [2]

$$p_{\mathrm{water}} = P_{\mathrm{H}}\left(1 - \frac{\gamma\mu}{2}\right) + \gamma\rho e \tag{56}$$

where $\mu = \rho/\rho_0 - 1$, $\gamma = 0.5$, and

$$P_{\mathrm{H}} = \begin{cases} \frac{\rho_0 c_0^2 \mu(1+\mu)}{[1-(S-1)\mu]^2} & \mu > 0 \\ \rho_0 c_0^2 \mu & \mu < 0 \end{cases} \tag{57}$$

with $\rho_0 = 1000$ kg/m^3, $c_0 = 1480$ m/s and $S = 2.56$. In the SGSPM, the volumetric locking is not a concern in the simulation of water because the cell center quadrature in the staggered grid scheme is the reduced integration and is free from volumetric locking.

3.1.2. Particles for shell structures

The dynamic fracture of shell structures is simulated by shell particles and converted MPM particles, as shown in Fig. 8. The mapping scheme for shell structure particles should be consistent with that for fluid particles. And the cell crossing noise in the converted MPM particles should be eliminated. Therefore, the particles for shell structures are also calculated in the staggered grid scheme. In the step (1), the contribution of both MPM particles and shell particles are considered in the reconstruction of the quantities at cell centers. The mass and momentum at cell centers are given by

$$m_a = \sum_{s=1}^{n_{\mathrm{s}}} N_{as} m_s + \sum_{c=1}^{n_{\mathrm{c}}} N_{ac} m_c \tag{58}$$

$$\boldsymbol{p}_a = \sum_{s=1}^{n_{\mathrm{s}}} N_{as} m_s \boldsymbol{v}_s + \sum_{c=1}^{n_{\mathrm{c}}} N_{ac} m_c \boldsymbol{v}_c \tag{59}$$

where the subscript s denotes the variables associated with MPM particle s converted from shell particles and n_{s} is the total number of converted MPM particles. The forces at shell particle corners contributes to those at cell centers, namely,

$$\boldsymbol{f}_a^{\mathrm{int}} = \sum_{c=1}^{n_{\mathrm{c}}} N_{ac} \boldsymbol{f}_c^{\mathrm{int}} \tag{60}$$

$$\boldsymbol{f}_a^{\mathrm{ext}} = \sum_{c=1}^{n_{\mathrm{c}}} N_{ac} \boldsymbol{f}_c^{\mathrm{ext}} \tag{61}$$

where $\boldsymbol{f}_a^{\mathrm{int}}$ and $\boldsymbol{f}_a^{\mathrm{ext}}$ denote the internal and external forces at cell centers mapped from shell particle corners. Then, the mass and momentum at grid nodes are obtained by Eqs. (37) and (38). The internal and external forces at grid nodes are evaluated by

$$\boldsymbol{f}_I^{\mathrm{int}} = -\sum_{a=1}^{n_{\mathrm{a}}} \nabla N_{Ia} \cdot \boldsymbol{\sigma}_a V_a + \sum_{a=1}^{n_{\mathrm{a}}} N_{Ia} \boldsymbol{f}_a^{\mathrm{int}} \tag{62}$$

$$\boldsymbol{f}_I^{\mathrm{ext}} = \sum_{a=1}^{n_{\mathrm{a}}} N_{Ia} m_a \boldsymbol{b}_a + \sum_{a=1}^{n_{\mathrm{a}}} N_{Ia} \boldsymbol{f}_a^{\mathrm{ext}} \tag{63}$$

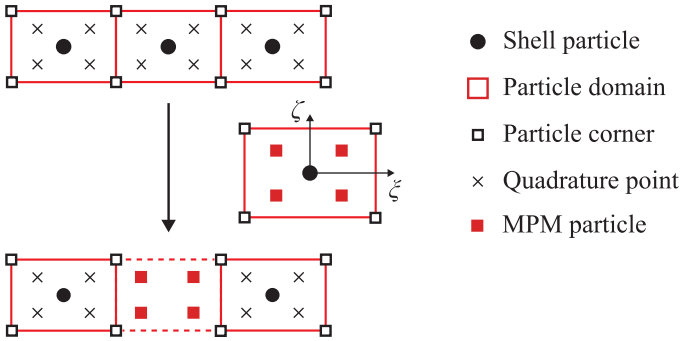


Fig. 9. Conversion of a shell particle to MPM particles.

In the step (3), the converted MPM particles are updated by Eqs. (49)–(52). To guarantee the continuity of displacement between shell particles and converted MPM particles, the velocity and position of shell particle corners are updated by the same scheme, namely,

$$\boldsymbol{v}_c^{n+1/2} = \boldsymbol{v}_c^{n-1/2} + \sum_{a=1}^{n_a} N_{ac}\boldsymbol{a}_a^n \Delta t^n \tag{64}$$

$$\boldsymbol{x}_c^{n+1} = \boldsymbol{x}_c^n + \sum_{a=1}^{n_a} N_{ac}\boldsymbol{v}_a^{n+1/2} \Delta t^{n+1/2} \tag{65}$$

The strain rate and vorticity rate of shell particles are evaluated by Eqs. (21) and (22). The locking treatments presented in the work of Li et al. [56] are also employed in shell particles.

3.2. Conversion algorithm

To model dynamic fracture of shell structures, a conversion algorithm is proposed to adaptively convert shell particles under extreme deformation into MPM particles. Subsequently, the failure treatment of MPM particles is utilized to simulate the fracture. In the MPM, the equivalent plastic strain failure criterion is generally employed. Once the equivalent plastic strain of the MPM particles reaches the failure strain $\bar{\varepsilon}_{\text{fail}}$ of the material, the deviatoric components of the stress tensor are set to zero. Therefore, the equivalent plastic strain conversion criterion is employed in the conversion algorithm. Once the equivalent plastic strain of a quadrature point exceeds the threshold, the shell particle is converted into MPM particles. The threshold for conversion is referred to as the conversion strain

$$\bar{\varepsilon}_{\text{convert}} = \beta \bar{\varepsilon}_{\text{fail}} \tag{66}$$

where β is a constant that ranges from 0.6 to 0.9 in this work.

As shown in Fig. 9, the middle shell particle satisfies the conversion criterion and is converted into $2 \times 2 \times 2$ MPM particles. In a background grid cell, it is common that two MPM particles are uniformly placed in each direction. The characteristic lengths of a shell particle in three directions, l_ξ, l_η and l_ζ, are calculated before conversion. Integers n_ξ, n_η and n_ζ are obtained after dividing the lengths by the background grid cell size and rounding. Therefore, the shell particle is removed and replaced by $2n_\xi \times 2n_\eta \times 2n_\zeta$ MPM particles.

To obtain the information of converted MPM particles, the shell particle in natural coordinate system is divided into eight quadrants, and $n_\xi \times n_\eta \times n_\zeta$ MPM particles are uniformly placed in each quadrant. The natural coordinates of MPM particles can be obtained and used to calculate the global coordinates. As shown in Fig. 9, the constants for the middle shell particle are $n_\xi = n_\eta = n_\zeta = 1$. The natural coordinates of converted MPM particles are $(\pm 0.5, \pm 0.5, \pm 0.5)$, so that the global coordinates are given by

$$\boldsymbol{x}_s = \sum_{c=1}^{8} N_c(\pm 0.5, \pm 0.5, \pm 0.5)\boldsymbol{x}_c \tag{67}$$

The mass of replaced shell particle is equally averaged to MPM particles. The history quantities (stress, strain, etc.) of MPM particles are set as those of the adjacent quadrature point in replaced shell particle. The velocity field in the material domain is characterized by the velocities at the shell particle corners, so the velocities of MPM particles are set to those of the adjacent shell particle corners to guarantee momentum conservation.

The remaining shell particles and converted MPM particles are combined together to model the dynamic fracture of shell structures. The momentum equations are solved on the same background grid and both types of particles are updated by the same mapping scheme. Coupling between the remaining shell particles and converted MPM particles is naturally implemented without additional algorithms. The advantages of shell particles to simulate bending deformation and MPM particles to model fracture are combined by the conversion algorithm.

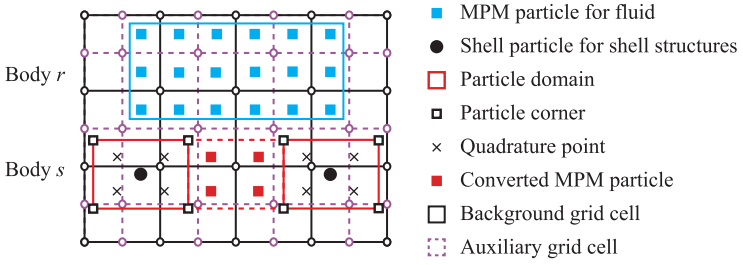


Fig. 10. Contact between particles for shell structures and particles for fluid.

4. Local multi-mesh contact method

A local multi-mesh contact method is presented for the interaction between the fluid and shell structures. The fluid is modeled by MPM particles. The shell structures are modeled by shell particles and converted MPM particles. They share the same nodal DOFs and have a consistent computational framework, which makes the contact method based on the staggered grid easy to be implemented.

The interaction of fluid body r and shell structure body s is shown in Fig. 10. In each time step, the velocities of two bodies at the same background grid node can be obtained after independently updating body r and body s. Therefore, the contact state of each grid node can be detected by its velocities of two bodies, and contact forces can be imposed between two bodies to prevent penetration if contact occurs.

4.1. Contact detection

The contact detection is based on the velocity fields of two bodies at background grid nodes and distances between two bodies at auxiliary grid nodes. The velocity of body $b(b = r, s)$ at background grid node I can be obtained by

$$v_{iI}^{b,n-1/2} = \frac{p_{iI}^{b,n-1/2}}{m_I^{b,n}} \tag{68}$$

The process of the contact detection consists of two steps. First, potential contact regions are identified, and multiple grid nodes are generated. If the velocity of background grid node I is influenced by the two bodies simultaneously, then both body r and body s are in the support domain of background grid node I. The grid node I is then duplicated into multiple grid nodes I_r and I_s, which store the information of body r and body s, respectively. Only a subset of the background grid nodes are duplicated into multiple grid nodes in each time step, significantly reducing computational cost.

Second, contact conditions are checked. Contact may take place in the vicinity of background grid node I if

$$(v_{iI}^{r,n-1/2} - v_{iI}^{s,n-1/2}) n_{iI}^{r,n} > 0 \tag{69}$$

where $n_{iI}^{r,n}$ is the unit outward normal on the surface of body r at background grid node I. The $n_{iI}^{r,n}$ of fluid body is calculated by the gradient of mass of auxiliary grid nodes [54] as

$$n_{iI}^{r,n} = \frac{1}{\left|\sum_{a=1}^{n_a} N_{Ia,i} m_a\right|} \sum_{a=1}^{n_a} N_{Ia,i} m_a \tag{70}$$

or by $n_{iI}^{r,n} = -n_{iI}^{s,n}$, where $n_{iI}^{s,n}$ is the unit outward normal on the surface of shell structure body at background grid node I. For remaining shell particles of body s, the unit outward normal at auxiliary grid node a, $n_{ia}^{s,n}$, is obtained by mapping the normal vectors on the surfaces of shell particles. Then, the $n_{iI}^{s,n}$ is calculated by mapping the $n_{ia}^{s,n}$ from auxiliary grid node a to background grid node I. For the converted MPM particles of body s, the $n_{iI}^{s,n}$ is given by Eq. (70).

The condition (69) can be rewritten in a momentum form as

$$(m_I^{s,n} p_{iI}^{r,n-1/2} - m_I^{r,n} p_{iI}^{s,n-1/2}) n_{iI}^{r,n} > 0 \tag{71}$$

The distances between two bodies at auxiliary grid nodes are also considered in contact detection. Contact may take place at background grid nodes of cell a if

$$D_a^{r,s} < \lambda d_c \tag{72}$$

where $D_a^{r,s}$ is the minimum distance between two bodies in the direction of normal vector at auxiliary grid node a, d_c is the cell size and λ is a specified distance factor.

In conclusion, if Eq. (71) is satisfied at background grid node I and Eq. (72) is satisfied at the cell in which node I is located, contact between two bodies occurs at node I.

In addition, the sizes of shell particle domains should not exceed three grid cell sizes to ensure proper contact detection. During pre-processing, one to three layers of background grid cells are usually occupied by the shell particles in each in-plane direction.

4.2. Contact force

Contact force should be imposed to prevent penetration when contact occurs at background grid node I. Then, the momentum p_{iI}^{b} of body $b(b = r, s)$ is given as

$$p_{iI}^{b,n+1/2} = \bar{p}_{iI}^{b,n+1/2} + f_{iI}^{b,c,n}\Delta t^{n} \tag{73}$$

where

$$\bar{p}_{iI}^{b,n+1/2} = p_{iI}^{b,n-1/2} + f_{iI}^{b,n}\Delta t^{n} \tag{74}$$

is the trial momentum and $f_{iI}^{b,c,n}$ is the contact force applied on body b at time t^{n}.

The momentum p_{iI}^{b} should satisfy the impenetrability condition

$$(m_I^{s,n} p_{iI}^{r,n+1/2} - m_I^{r,n} p_{iI}^{s,n+1/2}) n_{iI}^{r,n} = 0 \tag{75}$$

Substituting Eq. (73) into Eq. (75), the normal contact force $f_I^{\mathrm{nor},n} = f_{iI}^{r,c,n} n_{iI}^{r,n} = -f_{iI}^{s,c,n} n_{iI}^{r,n}$ is obtained as

$$f_I^{\mathrm{nor},n} = -\frac{(m_I^{s,n} \bar{p}_{iI}^{r,n+1/2} - m_I^{r,n} \bar{p}_{iI}^{s,n+1/2}) n_{iI}^{r,n}}{(m_I^{r,n} + m_I^{s,n})\Delta t^{n}} = f_{I,1}^{\mathrm{nor},n} + f_{I,2}^{\mathrm{nor},n} \tag{76}$$

where

$$f_{I,1}^{\mathrm{nor},n} = -\frac{(m_I^{s,n} p_{iI}^{r,n-1/2} - m_I^{r,n} p_{iI}^{s,n-1/2}) n_{iI}^{r,n}}{(m_I^{r,n} + m_I^{s,n})\Delta t^{n}} \tag{77}$$

$$f_{I,2}^{\mathrm{nor},n} = -\frac{(m_I^{s,n} f_{iI}^{r,n} - m_I^{r,n} f_{iI}^{s,n}) n_{iI}^{r,n}}{m_I^{r,n} + m_I^{s,n}} \tag{78}$$

For stick contact, the non-slip condition is

$$(m_I^{s,n} p_{iI}^{r,n+1/2} - m_I^{r,n} p_{iI}^{s,n+1/2}) t_{iI}^{r,n} = 0 \tag{79}$$

Substituting Eq. (73) into Eq. (79), the tangential contact force $f_I^{\mathrm{stick},n} = f_{iI}^{r,c,n} t_{iI}^{r,n} = -f_{iI}^{s,c,n} t_{iI}^{r,n}$ is obtained as

$$f_I^{\mathrm{stick},n} = \frac{(m_I^{s,n} p_{iI}^{r,n-1/2} - m_I^{r,n} p_{iI}^{s,n-1/2}) t_{iI}^{r,n}}{(m_I^{r,n} + m_I^{s,n})\Delta t^{n}} + \frac{(m_I^{s,n} f_{iI}^{r,n} - m_I^{r,n} f_{iI}^{s,n}) t_{iI}^{r,n}}{m_I^{r,n} + m_I^{s,n}} \tag{80}$$

where

$$t_{iI}^{r,n} = \frac{(v_{iI}^{r,n-1/2} - v_{iI}^{s,n-1/2}) - (v_{jI}^{r,n-1/2} - v_{jI}^{s,n-1/2}) n_{jI}^{r,n} n_{iI}^{r,n}}{\left|(v_{iI}^{r,n-1/2} - v_{iI}^{s,n-1/2}) - (v_{jI}^{r,n-1/2} - v_{jI}^{s,n-1/2}) n_{jI}^{r,n} n_{iI}^{r,n}\right|} \tag{81}$$

is the unit tangent at grid node I. For slip contact, the Coulomb friction model can be adopted. The friction force is limited to $\mu \left\| f_I^{\mathrm{nor},n} \right\|$, where μ is the friction coefficient, namely

$$f_I^{\tan,n} = \min(\mu \| f_I^{\mathrm{nor},n} \|, \| f_I^{\mathrm{stick},n} \|) \tag{82}$$

Finally, the contact force for body b is expressed as

$$f_{iI}^{b,c,n} = f_I^{\mathrm{nor},n} n_{iI}^{b,n} + f_I^{\tan,n} t_{iI}^{b,n} \tag{83}$$

which can be applied to many engineering problems. In this work, only the normal contact force is considered for the problem of structural damage subjected to underwater explosion. In the examples in Section 6, the friction coefficient is set to 0 and friction force is ignored.

The impenetrability condition Eq. (75) may not be satisfied at the beginning of each time step if it is imposed at the end of the previous time step, because the background grid is reset in the step (4). The violation would cause disturbance to the system [24]. To eliminate the artificial disturbance, after mapping mass and momentum from particles to background grid by auxiliary grid, $f_{I,1}^{\mathrm{nor},n}$ is imposed to adjust the background grid nodal momentum $p_{iI}^{r,n-1/2}$ to

$$\tilde{p}_{iI}^{r,n-1/2} = p_{iI}^{r,n-1/2} + f_{I,1}^{\mathrm{nor},n} n_{iI}^{r,n} \Delta t^{n} \tag{84}$$

The forces cause the acceleration at adjacent auxiliary grid nodes to be

$$a_{ia}^{s} = \sum_{I=1}^{8} N_{Ia} f_{I,1}^{\mathrm{nor},n} n_{iI}^{s,n} / m_I^{s,n} \tag{85}$$

Then, the velocity of the contact particle corner in body s is adjusted to

$$\tilde{v}_{ic}^{s,n-1/2} = v_{ic}^{s,n-1/2} + \sum_{a=1}^{n_a} N_{ac} a_{ia}^{s} \Delta t^{n} \tag{86}$$

5. Algorithm summary

The overall computational process of the SGSPM is summarized as follows:

1. Reconstruct the mass and momentum of cell centers from particles by Eqs. (58) and (59); Calculate those at background grid nodes from cell centers by Eqs. (37) and (38); Impose boundary conditions.
2. Detect contact state of each grid node. If Eqs. (71) and (72) are satisfied, the two bodies contact at the grid node I.
3. Adjust the momenta of contact grid nodes by Eq. (84) and the velocities of contact shell particle corners by Eq. (86).
4. Calculate the strain and vorticity increments of cell centers and map the increments to MPM particles by Eqs. (47), (48), (51) and (52); Calculate the increments of shell particles by Eqs. (21) and (22), and modify the strain increment by the ANS and EAS methods.
5. Update the stress of MPM particles and shell particles; Reconstruct the stress and forces of cell centers by Eqs. (43), (44), (60) and (61); Calculate grid nodal force by Eqs. (62) and (63).
6. For contact grid nodes, calculate the second term of the normal contact force by Eq. (78) and the tangential contact force by Eq. (82); Add the contact forces to nodal force.
7. Integrate momentum equations on background grid.
8. Map the updated acceleration and velocity to cell centers by Eqs. (45) and (46); Update the velocity and position of MPM particles and shell particle corners by the acceleration and velocity of cell centers, Eqs. (49), (50), (64) and (65).
9. Convert failed and distorted shell particles into MPM particles based on the conversion algorithm.

Remark: The key improvement of the SGSPM is to change the mapping scheme between particles and background grid nodes. With the staggered grid scheme, the cell crossing noise in the particles for fluid is eliminated. The conversion algorithm brings the ability to simulate dynamic fracture of shell structures. The fluid–structure interaction is implemented by the local multi-mesh contact method. Therefore, SGSPM is a promising method to simulate structural damage subjected to underwater explosion.

6. Numerical examples

In this section, the ability of the SGSPM to model the large deformation of shell structures is illustrated by the example of full hemispherical shell. The capacity to simulate the dynamic fracture of shell structures is verified by the penetration of a thin plate. And then, the large deformation of a plate subjected to underwater explosion is modeled to demonstrate that the SGSPM is capable of eliminating the cell crossing noise. Finally, the SGSPM is applied to simulate the fragmentation of a plate and structural damage of a ship hull subjected to contact underwater explosion.

6.1. Full hemispherical shell

Full hemispherical shell [60] is a test to verify the ability to simulate the large deformation of shell structures. As shown in Fig. 11, the shell has a radius of $R = 10.0$ mm and a thickness of $t = 0.5$ mm. The strength model of the shell is described by the elasto–plastic constitutive law with linear isotropic hardening. The material has a Young's modulus of $E = 10$ MPa, a Poisson's ratio of $\nu = 0.2$, an initial yield stress of $\sigma_{y0} = 0.2$ MPa and a plastic hardening modulus of $H_{iso} = 9$ MPa. Four central symmetry concentrated loads are applied to the shell.

Since the SGSPM is implemented as an explicit scheme for dynamic problems, this quasi-static problem is studied using the dynamic relaxation process with artificial damping. In the dynamic relaxation process, the external load F increases linearly to the specified value F_{spe}, namely

$$F = \begin{cases} \frac{t}{0.9t_e} F_{spe} & 0 \le t \le 0.9t_e \\ F_{spe} & 0.9t_e \le t \le t_e \end{cases} \tag{87}$$

where t is current time and t_e is the end time of simulation. To ensure that the deformation reaches equilibrium as quickly as possible, an artificial damping force $\boldsymbol{f}_c^{damp}$ is applied to the shell particle corners

$$\boldsymbol{f}_c^{damp} = -\eta \boldsymbol{v}_c \tag{88}$$

where η is the artificial damping factor. In this example, $t_e = 0.1$ms, $\eta = 5\times10^{-8}$ and the density of material is set to $\rho = 1\times10^{-9}$g/mm^3.

As shown in Fig. 11, the 1/4 model is adopted for simulations due to symmetry and is discretized into 12×12 shell particles. The background grid cell size is 0.25 mm. When $F = 0.04$ kN, the deformed configuration of the shell is illustrated in Fig. 12. The contours of equivalent plastic strain and von Mises stress obtained by SGSPM and SSMPM are shown in Fig. 12(a) and (c). As discussed in Section 2.3, MPM particles are affected by cell crossing noise, whereas shell particles are not. Therefore, the contours obtained by SGSPM and SSMPM are consistent. The contours obtained by ABAQUS are shown in Fig. 12(b) and (d). The equivalent plastic strain contour of SGSPM agrees well with that of ABAQUS, but there are some differences in their von Mises stress contours due to their different post-processing display methods used. In the contours of SGSPM, the maximum von Mises stress of quadrature points is plotted in each shell particle. However in ABAQUS, the von Mises stress in each element is reconstructed. The maximum

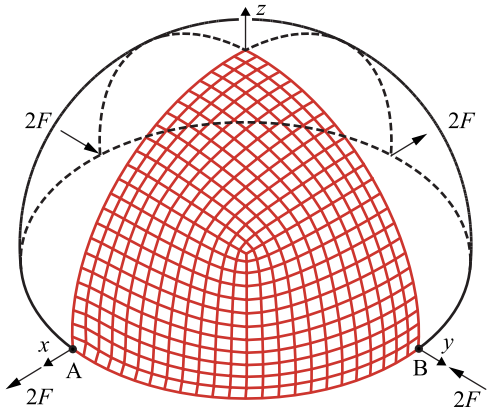


Fig. 11. Diagram and discretization of full hemispherical shell.

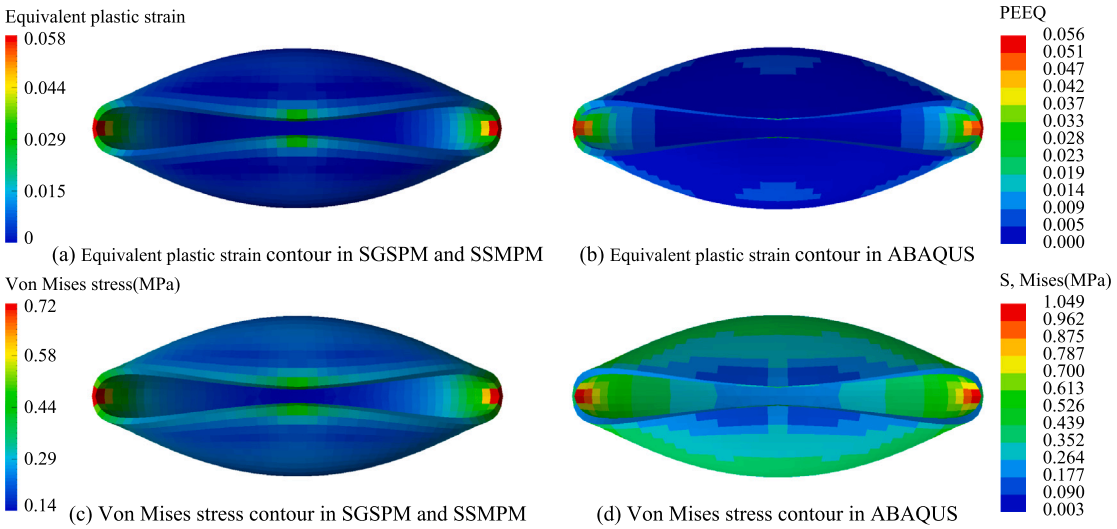


Fig. 12. Contours of equivalent plastic strain and von Mises stress obtained by SGSPM, SSMPM and ABAQUS.

Von Mises stress, $\sigma_{\text{Mises}}^{\max} = 0.72$ MPa, can be calculated by substituting the maximum effective plastic strain, $\varepsilon_{\text{p}}^{\max} = 0.058$, into the elasto–plastic constitutive law with linear isotropic hardening in this section, namely,

$$\sigma_{\text{Mises}}^{\max} = \sigma_{\text{y0}} + H_{\text{iso}}\varepsilon_{\text{p}}^{\max} \tag{89}$$

which confirms that the von Mises stress contour of SGSPM is also reasonable.

The inner and outer surfaces of shell structures are explicitly represented due to the hexahedral particle domain of shell particles. The radial displacements at the inner and outer points of A and B can be obtained when the shell is dynamically relaxed to the equilibrium state. The curves of load F versus the displacements obtained by SGSPM and SSMPM are illustrated in Fig. 13. The curves given by the literature [60] (represented as Kli06) and the FEM with the CSS8 element of ABAQUS (denoted as Reference) are also shown. The results of SGSPM and SSMPM show good agreement with these reference results. When the background grid size is 0.5 mm, the results of SGSPM are identical to those obtained with a grid size of 0.25 mm, so they are omitted. This example demonstrates the ability of SGSPM for simulating large deformation of shell structures.

6.2. Penetration of a thin plate by a ball

To verify the capacity of SGSPM to simulate the dynamic fracture of shell structures, the penetration of a thin circular plate by a ball is modeled in this section. The circular plate has a diameter of 178 mm and a thickness of 1 mm. The ball has a diameter of 10 mm and an initial velocity of 200 m/s. The direction of impact is normal to the plate.

As shown in Fig. 14, the 1/4 model is used due to symmetry. The plate is discretized into 9048 shell particles. The ball is discretized into 8388 MPM particles. The background grid size is 0.5 mm. The friction is neglected and the contact distance factor

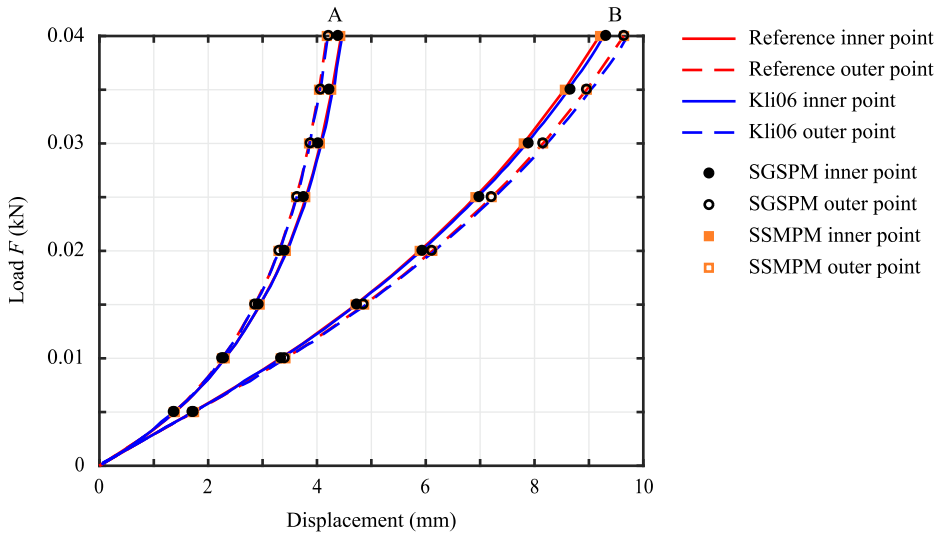


Fig. 13. Plot of load F v.s. displacements at the inner points and outer points of A and B.



Fig. 14. Diagram for the plate and ball.

Table 1
Material constants of steel.

$\rho\,(\mathrm{kg/m^3})$	E (GPa)	υ	A (MPa)	B (MPa)	n
7850	200.0	0.30	600.0	275.0	0.36

is set to 1.0. The strength model of the steel ball and steel plate is described by the elasto–plastic constitutive law with isotropic hardening

$$\sigma_y = A + B\varepsilon_{\mathrm{p}}^{n} \tag{90}$$

where A, B and n are the material constants, σ_y is the flow stress and ε_{p} is the effective plastic strain. The material constants are listed in Table 1 from the experiment [61]. The failure of MPM particles is considered by setting the deviatoric components of the stress tensor to zero when the effective plastic strain reaches the failure strain $\bar{\varepsilon}_{\mathrm{fail}} = 0.45$. Shell particles are converted into MPM particles when the equivalent plastic strain of a quadrature point exceeds the conversion strain $\bar{\varepsilon}_{\mathrm{convert}} = 0.3$.

The configurations in the penetration process are shown in Fig. 15. The shell particles under extreme deformation are adaptively converted into MPM particles and some MPM particles fail, which allows the plate to be perforated by the ball. In addition, the converted MPM particles are still coupled with remaining shell particles to simulate the same plate.

The residual velocities of the ball obtained by SGSPM is 88.2 m/s. The final deformed thin plates obtained by the experiment [61] and SGSPM are shown in Fig. 16, in which h is the height of the final deformed plate and D is the diameter of penetrated hole. The value of h/D obtained by simulation is 0.82 which is consistent with the experiment result 0.84. When the background grid size is 1 mm, the results of SGSPM are identical to those obtained with a grid size of 0.5 mm. The same results are obtained after rotating the model by 45° relative to the background grid. The advantages of the shell particles to simulate bending deformation and the MPM particles to simulate fragmentation are combined in this example, which verifies the capacity of SGSPM to simulate the dynamic fracture of shell structures.

6.3. Large deformation of a plate subjected to underwater explosion

In this section, the large deformation of a plate subjected to underwater explosion is simulated to demonstrate the elimination of the cell crossing noise. Ramajeyathilagam and Vendhan [62] carried out the experiment. The size of the plate is 300 mm × 250 mm. The thickness of the plate is 2 mm. The TNT explosive has a mass of 23.4 g and is located at 150 mm below the center of the plate.

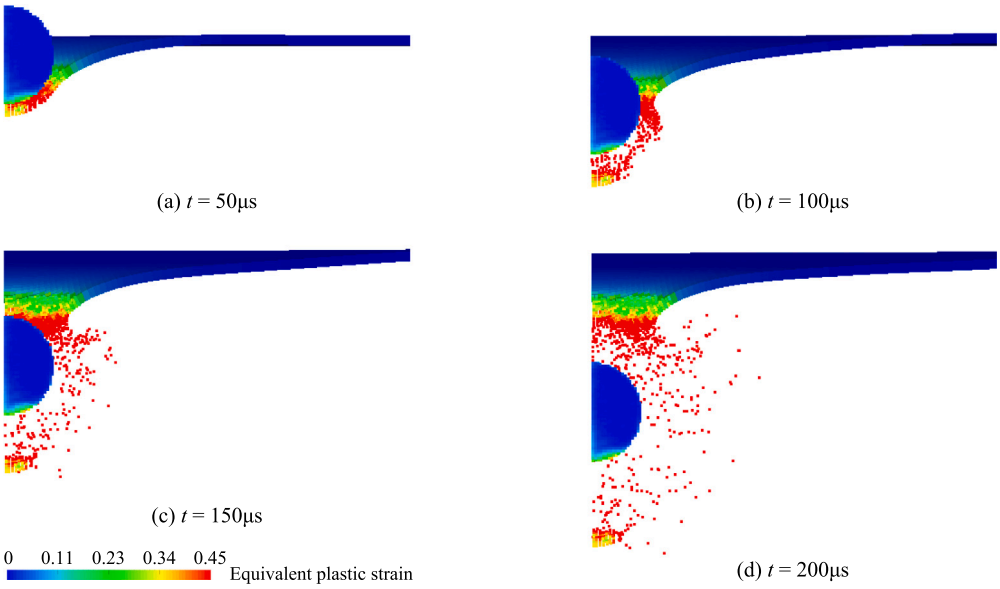


Fig. 15. Configurations in the penetration process.

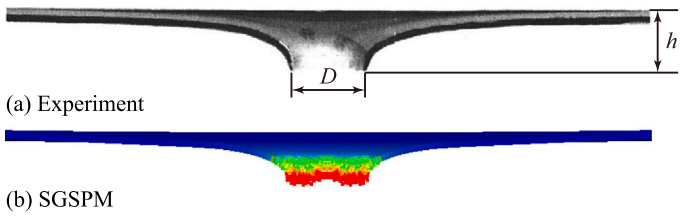


Fig. 16. Final deformed shape of the thin plate.

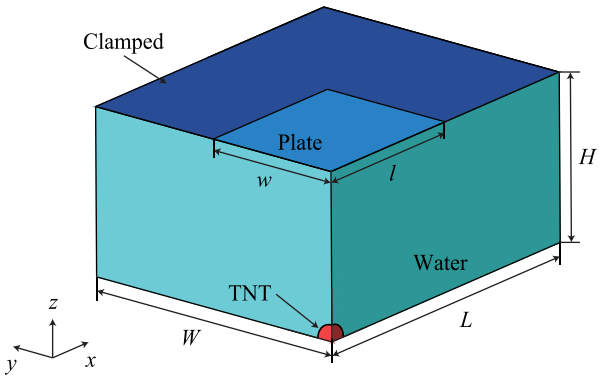


Fig. 17. Diagram of plate subjected to underwater explosion.

Due to symmetry, the first octant of the model is simulated, as shown in Fig. 17. The deformable part of the plate has a size of 150 mm × 125 mm and is discretized into 3000 shell particles. The rest of the plate is clamped. The fluid domain has a size of 300 mm × 250 mm × 150 mm and is discretized into 11,060,800 MPM particles. The background grid size is 2 mm. For the plate, the boundary conditions at $x = 0$ mm and $y = 0$ mm are symmetric boundaries. For the fluid, the boundary conditions at $x = 0$ mm, $y = 0$ mm and $z = 0$ mm are symmetric boundaries, and the surfaces of $x = 300$ mm and $y = 250$ mm are set as non-reflecting boundaries. The friction is neglected and the contact distance factor is set to 1.0.

The elasto–plastic constitutive law with isotropic hardening and Cowper–Symonds model

$$\sigma_y = (A + B\epsilon_{\mathrm{p}}) \left[1 + \left(\frac{\dot{\epsilon}_{\mathrm{p}}}{C}\right)^m\right] \tag{91}$$

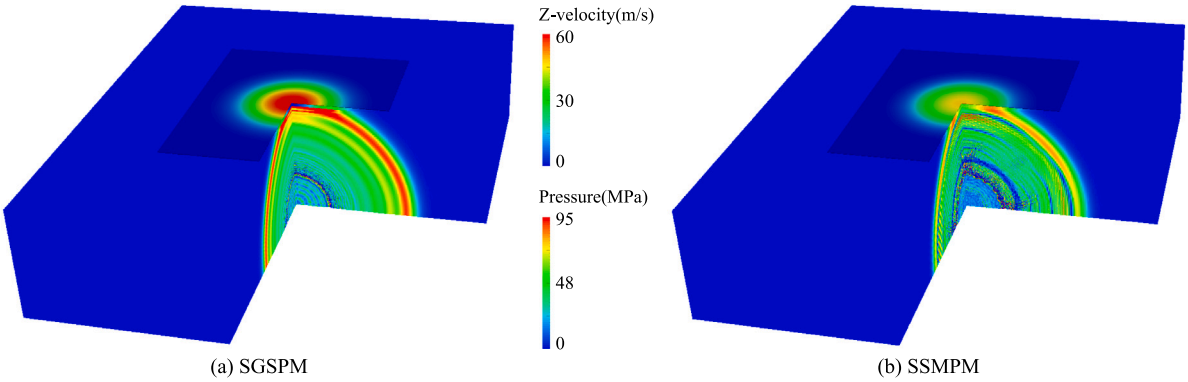


Fig. 18. Contours of fluid pressure and plate velocity at $t = 75$ μs.

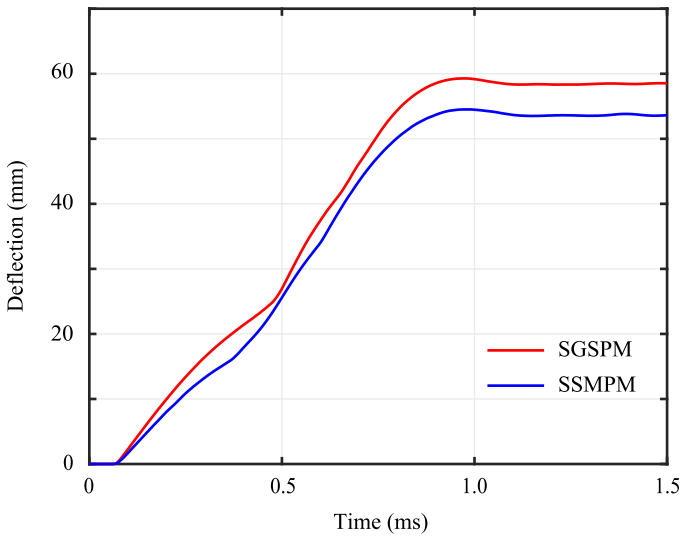


Fig. 19. Deflection history of the plate center.

is employed to model the steel plate [62], where $A = 300$ MPa, $B = 250$ MPa, $C = 40$ s^{-1} and $m = 5$. The Young's modulus and Poisson's ratio of the steel are 210 GPa and 0.3, respectively. The density of the steel is 7860 kg/m^3. The material of TNT and water are set the same as those in Section 3.1.1.

The pressure contour of the fluid and the velocity contour of the plate at $t = 75$ μs obtained by SGSPM and SSMPM are shown in Fig. 18. The shock wave generated by the underwater explosion arrives at the plate at this time. The upward velocity of the plate is generated due to the fluid–structure interaction. Severe numerical noise is evident in the shock wave obtained by SSMPM. In contrast, the shock wave obtained by SGSPM is relatively smooth, because the cell crossing noise is eliminated by the staggered grid scheme in the SGSPM.

Fig. 19 plots the deflection history of the plate center. The deflections of SGSPM and SSMPM finally reach stable values. However, the stable value of SSMPM is lower than that of SGSPM. The final deformed configurations and pressure contours of the plate are shown in Fig. 20. The plate has undergone large deformation, which can be seen from the deflection contours of simulations. The deformed configurations in the simulations are in good agreement with the experimental result. The pressure contour of the plate obtained by SGSPM is smoother than that obtained by SSMPM because the deformation of the plate is driven by the shock wave in the fluid and the fluid simulation of SGSPM is more accurate than that of SSMPM.

The final deflection along the short and long symmetry axes is given in Fig. 21. The final center deflections are listed in Table 2 to specifically compare the results of experiment and simulations. The results obtained by SSMPM and LS-DYNA [62] are slightly different from the experimental results. However, the center deflection of SGSPM is consistent with the experimental result with the relative error of 1.2%, and the deflection along the symmetry axes of SGSPM is in good agreement with the experimental results.

A mesh sensitivity analysis of SGSPM is further performed. The background grid cell sizes d_g are chosen as 4 mm, 2.5 mm, 2 mm and 1.5 mm, respectively. The final center deflections obtained by those simulations are 58.7 mm, 58.5 mm, 58.5 mm and 58.5 mm, respectively. The result for the cell size $d_g = 4$ mm is consistent with the experimental result. As the grid is refined, the

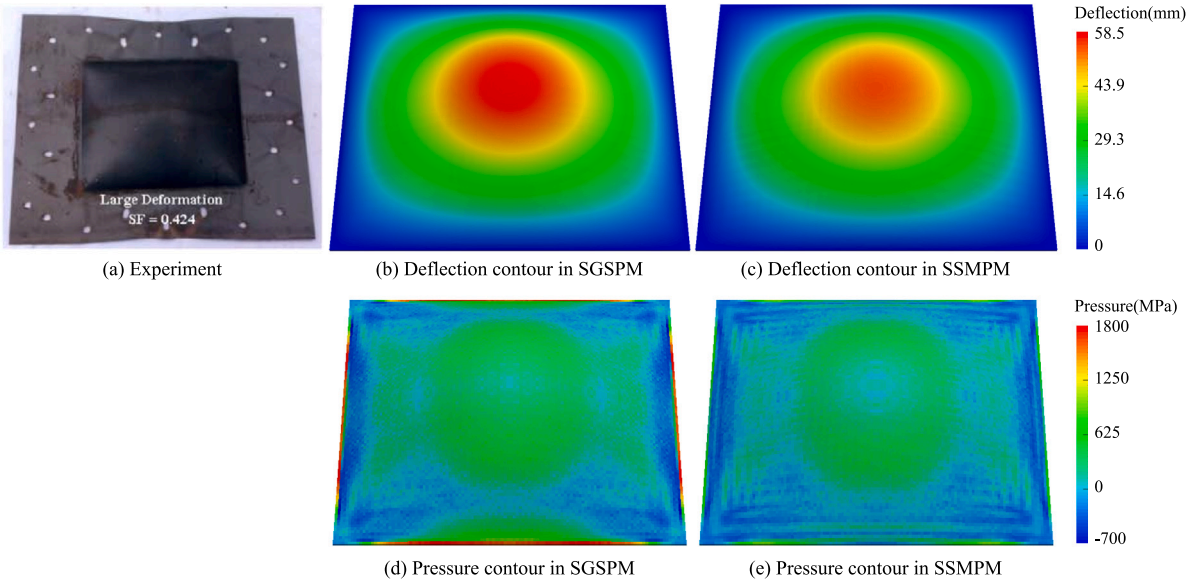


Fig. 20. Final deformed configurations and pressure contours of the plate.

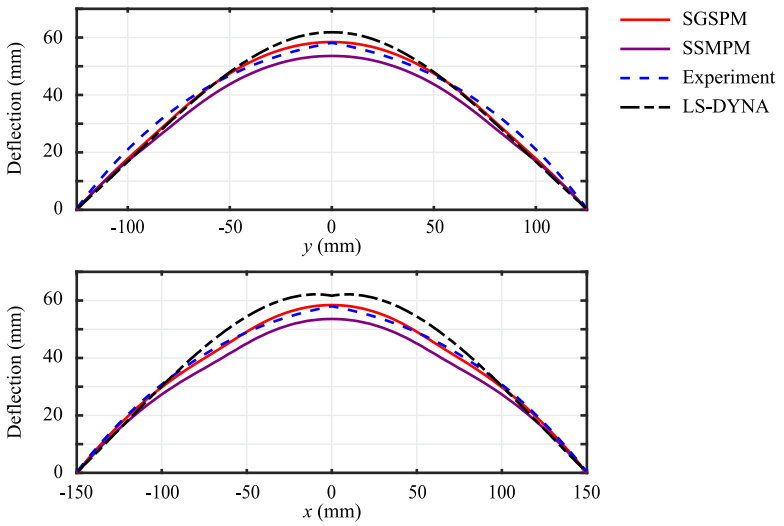


Fig. 21. Final deflection along the symmetry axes.

Table 2
Final center deflections.

	Experiment	SGSPM	SSMPM	LS-DYNA
Center deflection (mm)	57.8	58.5	53.5	61.6

results become more accurate and converge to 58.5 mm. This example demonstrates the elimination of the cell crossing noise in the SGSPM and verifies the accuracy of SGSPM in simulating shell structures subjected to underwater explosion.

6.4. Fragmentation of a plate subjected to contact underwater explosion

The SGSPM is applied to simulate the fragmentation of a plate subjected to contact underwater explosion in this section. Rajendran and Narasimhan [63] carried out the experiment. The circular plate has a radius of 145 mm and a thickness of 4 mm. The TNT explosive has a mass of 22.3 g and is right below the center of the plate.

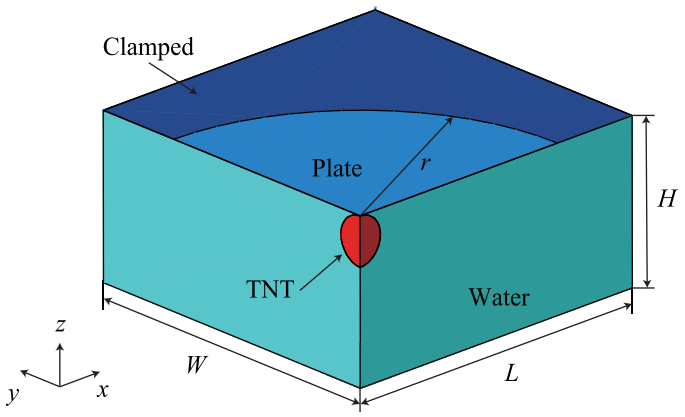


Fig. 22. Diagram of plate subjected to contact underwater explosion.

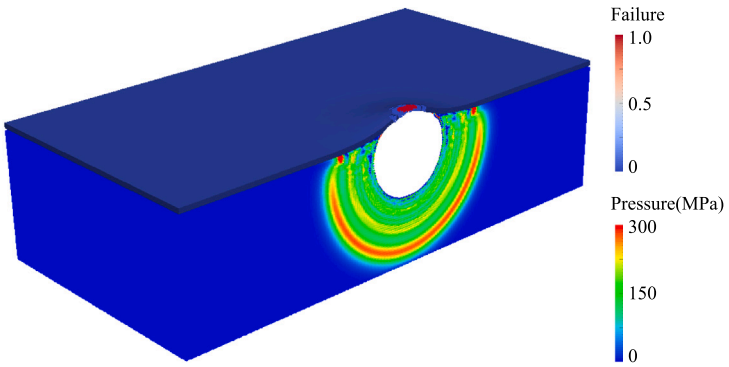


Fig. 23. Contours of water pressure and plate failure at $t = 30$ μs.

As shown in Fig. 22, the 1/4 model is simulated due to symmetry. The deformable part of the plate is discretized into 2476 shell particles. The rest of the plate is clamped. The fluid domain has a size of 200 mm × 200 mm × 100 mm and is discretized into 4,221,760 MPM particles. The background grid size is 2 mm. The boundary conditions at $x = 0$ mm and $y = 0$ mm are symmetric boundaries for the plate and fluid. The surfaces of $x = 200$ mm, $y = 200$ mm and $z = 0$ mm are set as non-reflecting boundaries for the fluid. The friction is neglected and the contact distance factor is set to 0.5.

The strength model of the steel plate [63] is described by the elasto–plastic constitutive law

$$\sigma_y = A(B + \varepsilon_{\mathrm{p}})^n \left[1 + \left(\frac{\dot{\varepsilon}_{\mathrm{p}}}{C}\right)^m\right] \tag{92}$$

where $A = 720$ MPa, $B = 0.025$, $n = 0.16$, $C = 70$ s^{-1} and $m = 8$. The Young's modulus and Poisson's ratio of the steel are 210 GPa and 0.3, respectively. The density of the steel is 7860 kg/m^3. The failure strain of the steel is $\bar{\varepsilon}_{\mathrm{fail}} = 0.18$. The deviatoric components of the stress tensor are set to zero when the effective plastic strain of MPM particles reaches the failure strain. Shell particles are converted into MPM particles when the equivalent plastic strain of a quadrature point exceeds the conversion strain $\bar{\varepsilon}_{\mathrm{convert}} = 0.15$. The material of TNT and water are set the same as those in Section 3.1.1.

The pressure contour of the water and the failure contour of the plate at $t = 30$ μs obtained by SGSPM are shown in Fig. 23. If the equivalent plastic strain of MPM particles reaches the failure strain, the failure value is set to 1 and the failure treatment in Section 3.2 is applied to the MPM particles. The failure value of shell particles and other MPM particles is set to 0. The explosive gas is represented by white particles to clearly distinguish between the plate and water. The explosive gas expands rapidly after the explosive is detonated. Large deformation and fragmentation occur in the center of the plate due to the fluid–structure interaction.

The process of the plate fracture obtained by SGSPM is shown in Fig. 24. Severe local bulge is generated and initial cracks are formed in the center of the plate at $t = 0.1$ ms. A petal-shaped fracture appears on the plate when the cracks propagate to $t = 0.5$ ms. The petal-shaped fracture rolls outwards and reaches a stable state at $t = 0.8$ ms. The process of the plate fracture obtained by SSMPM with the conversion algorithm in this work is shown in Fig. 25. The crack propagation process is sensitive to numerical noise. Obvious branching appears in the process of crack propagation due to the cell crossing noise.

Fig. 26 compares the final deformed configurations of the plate in the experiment, SGSPM and SSMPM. The radii of the crack (half of the maximum distance between crack tips) obtained by different methods are listed in Table 3. The relative error between

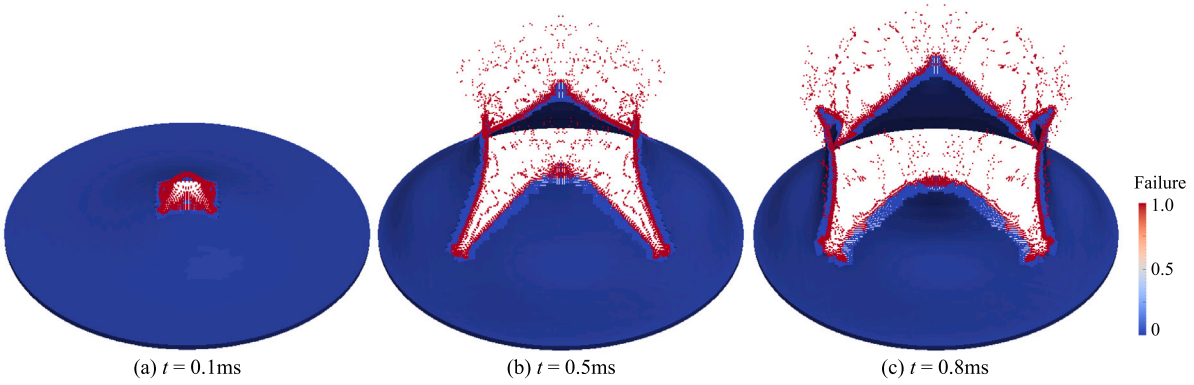


Fig. 24. Process of the plate fracture by SGSPM.

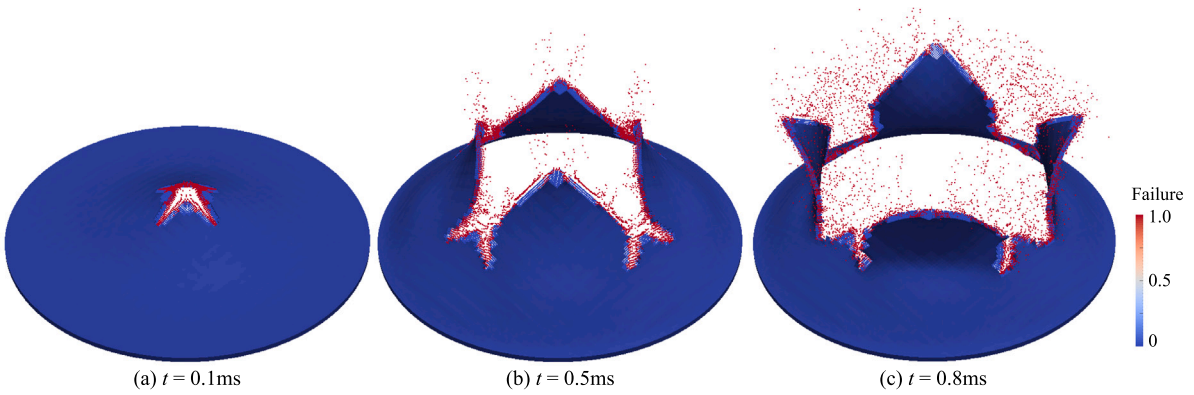


Fig. 25. Process of the plate fracture by SSMPM.

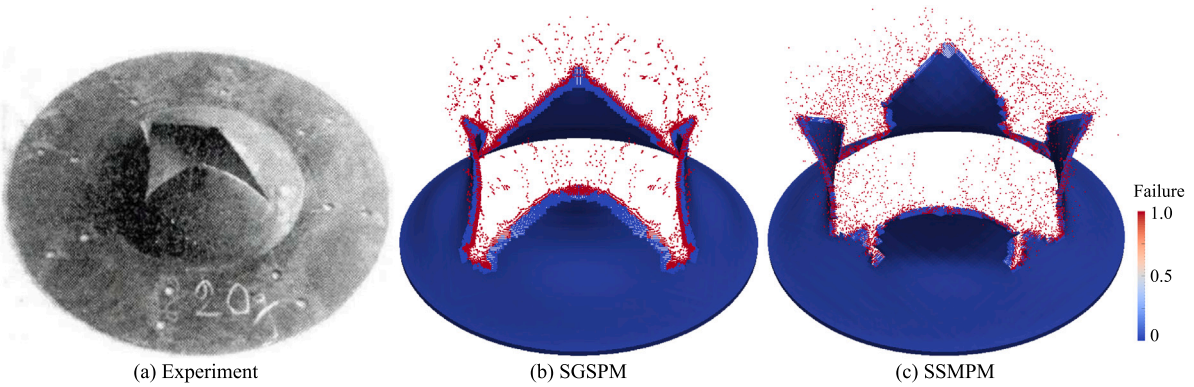


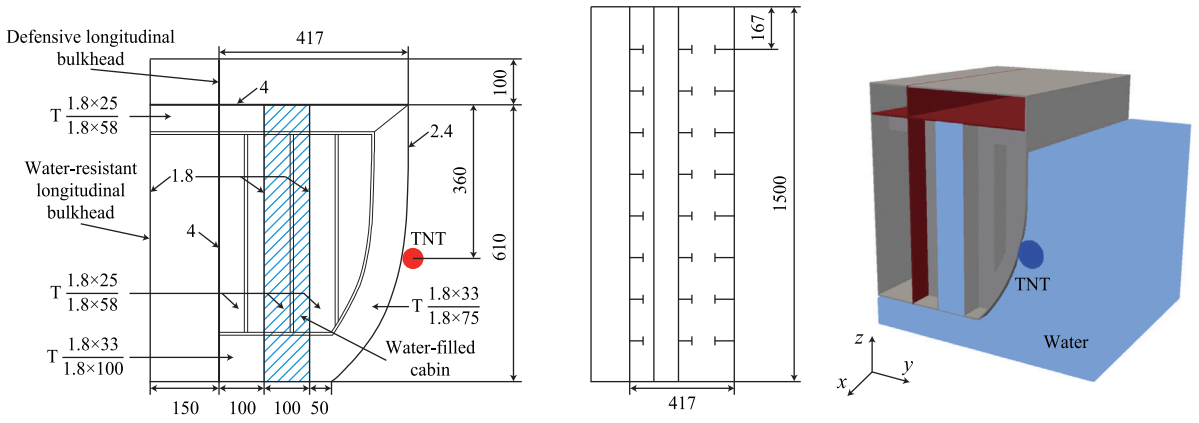
Fig. 26. Final deformed configurations of the plate.

the experiment and SGSPM is 7.7%. The result of SSMPM is 85.3 mm (considering the start of branching as crack tip) or 100.6 mm (considering the end of branching as crack tip). The result of SGSPM is significantly better than that of SSMPM because the SGSPM eliminates the cell crossing noise.

Slight circumferential failure is observed in the final configuration of SGSPM. This difference between the numerical and experimental results may be caused by the approximate description of cracks. In the present work, a collection of failure MPM particles is used to approximate cracks, which is simple and computationally efficient. In this example, the results of SGSPM are relatively accurate. A more accurate crack description method will be realized in the future work.

Table 3
Radius of the crack.

	Experiment	SGSPM	SSMPM	
			Start of branching	End of branching
Radius of the crack (mm)	120	110.8	85.3	100.6



(a) Cross section of ship hull and TNT (b) Planform of ship hull (c) Simulation model

Fig. 27. Diagram and simulation model of ship hull subjected to contact underwater explosion.

Table 4
Lengths of the hole on the outboard armor plate.

	Experiment	SGSPM
Longitudinal length (mm)	430	406
Vertical length (mm)	340	367

6.5. Structural damage of a ship hull subjected to contact underwater explosion

The SGSPM is applied to simulate the structural damage of a ship hull subjected to contact underwater explosion in this section. Zhu et al. [64] carried out the experiment. The diagram of the ship hull is shown in Fig. 27(a) and (b). The TNT explosive has a mass of 300 g.

As shown in Fig. 27(c), the 1/2 simplified model is simulated due to symmetry. The computational domain has a size of 750 mm × 850 mm × 850 mm. The ship hull is discretized into 177,703 shell particles. The fluid domain is discretized into 30,454,460 MPM particles. The background grid size is 4 mm. The boundary conditions at $x = 750$ mm are symmetric boundaries for the ship hull and fluid. The surfaces of $x = 0$ mm, $y = 0$ mm, $y = 850$ mm and $z = 0$ mm are set as non-reflecting boundaries for the fluid. The friction is neglected and the contact distance factor is set to 1.0.

The defensive longitudinal bulkhead and deck are made of low alloy steel, and the rest of the ship hull is made of carbon steel. The elasto–plastic constitutive law with isotropic hardening and Cowper–Symonds model in Section 6.3 is employed to model the steel. The parameters for the low alloy steel [64] are set as $A = 390$ MPa, $B = 1305$ MPa, $C = 6 \times 10^{-4}$ s^{-1} and $m = 50.8$, while the parameters for the carbon steel [64] are set as $A = 235$ MPa, $B = 250$ MPa, $C = 40.4$ s^{-1} and $m = 5$. The Young's modulus and Poisson's ratio of the steel are 210 GPa and 0.3, respectively. The density of the steel is 7860 kg/m^3. The failure strain of the steel is $\bar{\varepsilon}_{\text{fail}} = 0.28$. The deviatoric components of the stress tensor are set to zero when the effective plastic strain of MPM particles reaches the failure strain. Shell particles are converted into MPM particles when the equivalent plastic strain of a quadrature point exceeds the conversion strain $\bar{\varepsilon}_{\text{convert}} = 0.26$. The material of TNT and water are set the same as those in Section 3.1.1.

The pressure contour of the water and the equivalent plastic strain contour of the ship hull at $t = 0.1$ ms are shown in Fig. 28. After the explosive is detonated, the explosive gas expands rapidly and the strong shock wave is generated. The outboard armor plate of the ship hull is severely dented by the explosive gas and shock wave. The shell particles near the explosive gas are converted into MPM particles, and then some MPM particles fail. Fragments are formed from the failed MPM particles and fly towards the water-filled cabin along with the explosive gas.

Fig. 29 compares the final damaged configurations of the ship hull in the experiment and SGSPM. The concave region obtained by the SGSPM is in good agreement with the experimental result. The longitudinal and vertical lengths of the hole on the outboard armor plate are listed in Table 4, which shows the results of experiment and SGSPM are consistent.

The process of the ship hull damage obtained by the SGSPM is presented in Fig. 30. The outboard armor plate and the water-filled cabin are severely damaged, but no failure is found in the defensive and the water-resistant longitudinal bulkhead. This phenomenon

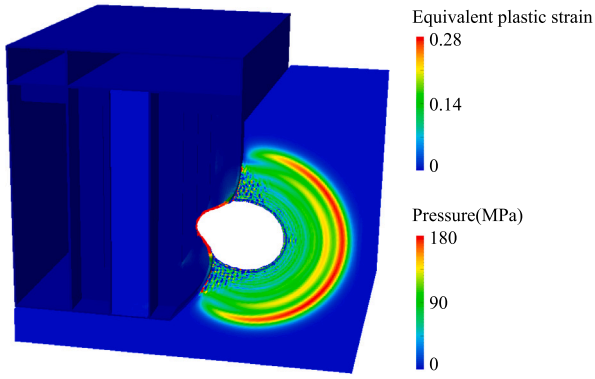


Fig. 28. Contours of water pressure and structural equivalent plastic strain at $t = 0.1$ ms.

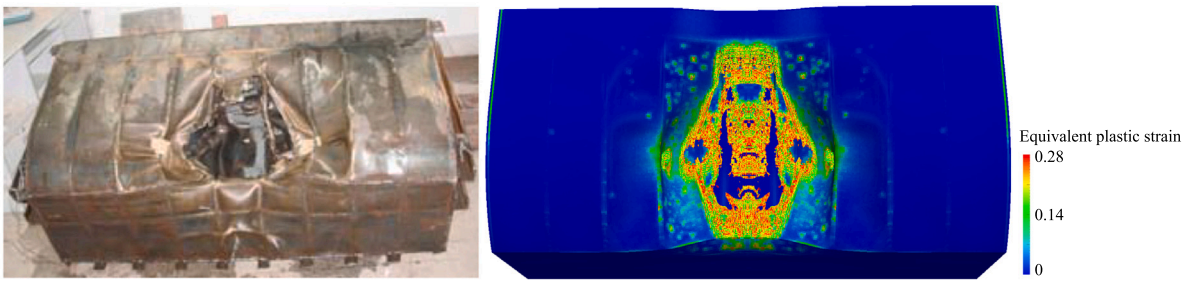


Fig. 29. Final damaged configurations of the ship hull.

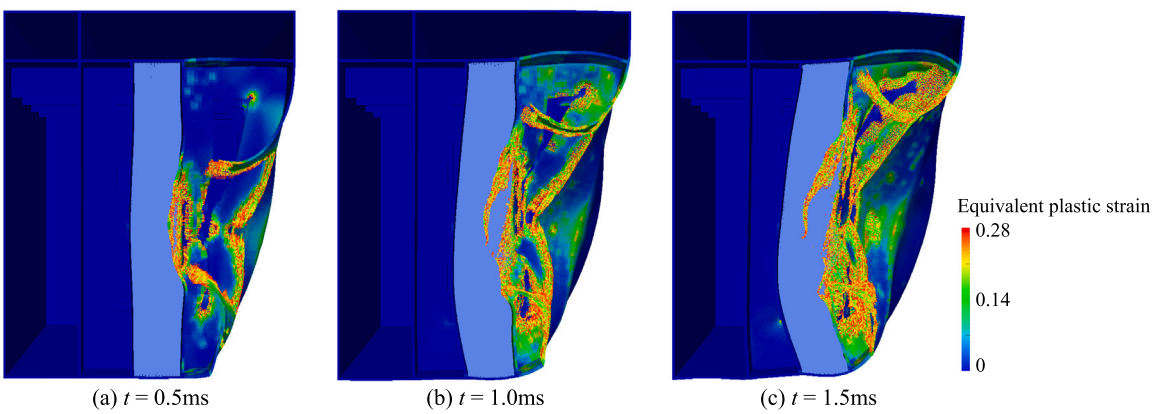


Fig. 30. Process of the ship hull damage.

is consistent with the experiment [64]. This example demonstrates the applicability of SGSPM in simulating structural damage of complex shell structures subjected to underwater explosion.

7. Conclusion

In this paper, a novel staggered grid shell particle method (SGSPM) is proposed to model the structural damage subjected to underwater explosion. The fluid in underwater explosion and shell structures are discretized by MPM particles and shell particles, respectively. The staggered grid scheme is introduced to eliminate the cell crossing noise and to improve the accuracy of fluid simulation. The conversion algorithm is employed to handle the dynamic fracture of shell structures. For shell structures, the advantages of the shell particles to simulate bending deformation and the MPM particles to simulate fragmentation are combined. Besides, a local multi-mesh contact method is presented in the staggered grid scheme for the fluid–structure interaction. In the

present work, a collection of failure MPM particles is used to approximate cracks, which is simple and computationally efficient. A more accurate crack description method will be implemented in the future work.

Five numerical examples are discussed to assess the performance of the SGSPM. The example of full hemispherical shell examines the ability to model the large deformation of shell structures. The penetration of a thin plate verifies the capability of simulating the dynamic fracture of shell structures. The large deformation of a plate subjected to underwater explosion demonstrates the elimination of the cell crossing noise. The fragmentation of a plate and structural damage of a ship hull subjected to contact underwater explosion demonstrate the applicability of simulating structural damage of shell structures subjected to underwater explosion. The numerical results fit well with the data in the literature and experiment, which indicates that the presented method is effective for modeling structural damage subjected to underwater explosion.

CRediT authorship contribution statement

Jiasheng Li: Writing – review & editing, Writing – original draft, Visualization, Validation, Software, Methodology, Investigation, Formal analysis, Data curation, Conceptualization. **Yong Liang:** Writing – review & editing, Software, Methodology. **Zhixin Zeng:** Writing – review & editing, Methodology. **Xiong Zhang:** Writing – review & editing, Supervision, Software, Resources, Project administration, Funding acquisition, Conceptualization.

Declaration of competing interest

We declare that we have no financial and personal relationships with other people or organizations that can inappropriately influence our work, there is no professional or other personal interest of any nature or kind in any product, service and/or company that could be construed as influencing the position presented in, or the review of, the manuscript.

Data availability

Data will be made available on request.

References

[1] D. Sulsky, Z. Chen, H. Schreyer, A particle method for history-dependent materials, Comput. Methods Appl. Mech. Engrg. 118 (1) (1994) 179–196.
[2] X. Zhang, Z. Chen, Y. Liu, The Material Point Method: A Continuum-Based Particle Method for Extreme Loading Cases, Academic Press, 2016.
[3] R.A. Gingold, J.J. Monaghan, Smoothed particle hydrodynamics: Theory and application to non-spherical stars, MNRAS 181 (2) (1977) 375–389.
[4] B. Maurel, A. Combescure, An SPH shell formulation for plasticity and fracture analysis in explicit dynamics, Internat. J. Numer. Methods Engrg. 76 (7) (2008) 949–971.
[5] T. Belytschko, Y.Y. Lu, L. Gu, Element-free Galerkin methods, Internat. J. Numer. Methods Engrg. 37 (2) (1994) 229–256.
[6] D. Wang, J.-S. Chen, Locking-free stabilized conforming nodal integration for meshfree mindlin-Reissner plate formulation, Comput. Methods Appl. Mech. Engrg. 193 (12) (2004) 1065–1083.
[7] D. Wang, J. Wu, An inherently consistent reproducing kernel gradient smoothing framework toward efficient Galerkin meshfree formulation with explicit quadrature, Comput. Methods Appl. Mech. Engrg. 349 (2019) 628–672.
[8] J. Wu, D. Wang, An accuracy analysis of Galerkin meshfree methods accounting for numerical integration, Comput. Methods Appl. Mech. Engrg. 375 (2021) 113631.
[9] J.-S. Chen, C. Pan, C.-T. Wu, W.K. Liu, Reproducing kernel particle methods for large deformation analysis of non-linear structures, Comput. Methods Appl. Mech. Engrg. 139 (1–4) (1996) 195–227.
[10] B.M. Donning, W.K. Liu, Meshless methods for shear-deformable beams and plates, Comput. Methods Appl. Mech. Engrg. 152 (1) (1998) 47–71.
[11] Y.X. Peng, A.M. Zhang, F.R. Ming, A thick shell model based on reproducing kernel particle method and its application in geometrically nonlinear analysis, Comput. Mech. 62 (3) (2018) 309–321.
[12] Y.-X. Peng, A.-M. Zhang, F.-R. Ming, A 3D meshfree crack propagation algorithm for the dynamic fracture in arbitrary curved shell, Comput. Methods Appl. Mech. Engrg. 367 (2020) 113139.
[13] S. Silling, Reformulation of elasticity theory for discontinuities and long-range forces, J. Mech. Phys. Solids 48 (1) (2000) 175–209.
[14] M. Behzadinasab, M. Alaydin, N. Trask, Y. Bazilevs, A general-purpose, inelastic, rotation-free Kirchhoff-Love shell formulation for peridynamics, Comput. Methods Appl. Mech. Engrg. 389 (2022) 114422.
[15] Q. Zhang, S. Li, A.-M. Zhang, Y. Peng, J. Yan, A peridynamic Reissner-Mindlin shell theory, Internat. J. Numer. Methods Engrg. 122 (1) (2021) 122–147.
[16] P. Karnakov, S. Litvinov, P. Koumoutsakos, A hybrid particle volume-of-fluid method for curvature estimation in multiphase flows, Int. J. Multiph. Flow 125 (2020) 103209.
[17] S.P. van der Pijl, A. Segal, C. Vuik, P. Wesseling, A mass-conserving level-set method for modelling of multi-phase flows, Internat. J. Numer. Methods Fluids 47 (4) (2005) 339–361.
[18] M. Liu, G. Liu, K. Lam, Z. Zong, Smoothed particle hydrodynamics for numerical simulation of underwater explosion, Comput. Mech. 30 (2003) 106–118.
[19] Y.-X. Peng, A.-M. Zhang, F.-R. Ming, Numerical simulation of structural damage subjected to the near-field underwater explosion based on SPH and RKPM, Ocean Eng. 222 (2021) 108576.
[20] P. Liu, Y. Liu, X. Zhang, Simulation of hyper-velocity impact on double honeycomb sandwich panel and its staggered improvement with internal-structure model, Int. J. Mech. Mater. Des. 12 (2) (2016) 241–254.
[21] S. Ma, X. Zhang, X. Qiu, Comparison study of MPM and SPH in modeling hypervelocity impact problems, Int. J. Impact Eng. 36 (2) (2009) 272–282.
[22] W. Gong, Y. Liu, X. Zhang, H. Ma, Numerical investigation on dynamical response of aluminum foam subject to hypervelocity impact with material point method, CMES - Comput. Model. Eng. Sci. 83 (5) (2012) 527–545.
[23] P. Huang, X. Zhang, S. Ma, H. Wang, Shared memory openmp parallelization of explicit MPM and its application to hypervelocity impact, CMES - Comput. Model. Eng. Sci. 38 (2) (2008) 119–148.
[24] P. Huang, X. Zhang, S. Ma, X. Huang, Contact algorithms for the material point method in impact and penetration simulation, Internat. J. Numer. Methods Engrg. 85 (4) (2011) 498–517.

[25] Z. Ma, X. Zhang, P. Huang, An object-oriented MPM framework for simulation of large deformation and contact of numerous grains, CMES - Comput. Model. Eng. Sci. 55 (1) (2010) 61–87.
[26] H. Tan, J.A. Nairn, Hierarchical, adaptive, material point method for dynamic energy release rate calculations, Comput. Methods Appl. Mech. Engrg. 191 (19–20) (2002) 2123–2137.
[27] Z. Chen, W. Hu, L. Shen, X. Xin, R. Brannon, An evaluation of the MPM for simulating dynamic failure with damage diffusion, Eng. Fract. Mech. 69 (17) (2002) 1873–1890.
[28] Y. Liang, B. Chandra, K. Soga, Shear band evolution and post-failure simulation by the extended material point method (XMPM) with localization detection and frictional self-contact, Comput. Methods Appl. Mech. Engrg. 390 (2022) 114530.
[29] C. Long, D. Zhang, C. Bronkhorst, G. Gray III, Representing ductile damage with the dual domain material point method, Comput. Methods Appl. Mech. Engrg. 300 (2016) 611–627.
[30] Y.-J. Cheon, H.-G. Kim, An adaptive material point method coupled with a phase-field fracture model for brittle materials, Internat. J. Numer. Methods Engrg. 120 (8) (2019) 987–1010.
[31] Z. Hu, H. Zhang, Y. Zheng, H. Ye, Phase-field implicit material point method with the convected particle domain interpolation for brittle-ductile failure transition in geomaterials involving finite deformation, Comput. Methods Appl. Mech. Engrg. 390 (2022) 114420.
[32] A. de Vaucorbeil, V.P. Nguyen, T.K. Mandal, Mesh objective simulations of large strain ductile fracture: A new nonlocal Johnson-Cook damage formulation for the total Lagrangian material point method, Comput. Methods Appl. Mech. Engrg. 389 (2022) 114388.
[33] D.Z. Zhang, Q. Zou, W.B. VanderHeyden, X. Ma, Material point method applied to multiphase flows, J. Comput. Phys. 227 (6) (2008) 3159–3173.
[34] F. Zhang, X. Zhang, K.Y. Sze, Y. Lian, Y. Liu, Incompressible material point method for free surface flow, J. Comput. Phys. 330 (2017) 92–110.
[35] S. Kularathna, K. Soga, Implicit formulation of material point method for analysis of incompressible materials, Comput. Methods Appl. Mech. Engrg. 313 (2017) 673–686.
[36] Y. Song, Y. Liu, X. Zhang, A transport point method for complex flow problems with free surface, Comput. Part. Mech. 7 (2020) 377–391.
[37] X. Zhao, D. Liang, M. Martinelli, Numerical simulations of dam-break floods with MPM, Procedia Eng. 175 (2017) 133–140.
[38] A. York, D. Sulsky, H. Schreyer, Fluid-membrane interaction based on the material point method, Internat. J. Numer. Methods Engrg. 48 (6) (2000) 901–924.
[39] S. Bandara, K. Soga, Coupling of soil deformation and pore fluid flow using material point method, Comput. Geotech. 63 (2015) 199–214.
[40] A. Gilmanov, S. Acharya, A hybrid immersed boundary and material point method for simulating 3D fluid-structure interaction problems, Internat. J. Numer. Methods Fluids 56 (12) (2008) 2151–2177.
[41] J. Li, Y. Hamamoto, Y. Liu, X. Zhang, Sloshing impact simulation with material point method and its experimental validations, Comput. & Fluids 103 (2014) 86–99.
[42] Y. Liu, H. Ye, H. Zhang, Y. Zheng, Coupling lattice Boltzmann and material point method for fluid-solid interaction problems involving massive deformation, Internat. J. Numer. Methods Engrg. 121 (24) (2020) 5546–5567.
[43] S.G. Bardenhagen, E.M. Kober, The Generalized Interpolation Material Point Method, CMES - Comput. Model. Eng. Sci. 5 (6) (2004) 477–495.
[44] P.C. Wallstedt, J. Guilkey, An evaluation of explicit time integration schemes for use with the generalized interpolation material point method, J. Comput. Phys. 227 (22) (2008) 9628–9642.
[45] M. Steffen, R.M. Kirby, M. Berzins, Analysis and reduction of quadrature errors in the material point method (MPM), Internat. J. Numer. Methods Engrg. 76 (6) (2008) 922–948.
[46] D.Z. Zhang, X. Ma, P.T. Giguere, Material point method enhanced by modified gradient of shape function, J. Comput. Phys. 230 (16) (2011) 6379–6398.
[47] A. Sadeghirad, R.M. Brannon, J. Burghardt, A convected particle domain interpolation technique to extend applicability of the material point method for problems involving massive deformations, Internat. J. Numer. Methods Engrg. 86 (12) (2011) 1435–1456.
[48] A. Sadeghirad, R. Brannon, J. Guilkey, Second-order convected particle domain interpolation (CPDI2) with enrichment for weak discontinuities at material interfaces, Internat. J. Numer. Methods Engrg. 95 (11) (2013) 928–952.
[49] M. Lu, J. Zhang, H. Zhang, Y. Zheng, Z. Chen, Time-discontinuous material point method for transient problems, Comput. Methods Appl. Mech. Engrg. 328 (2018) 663–685.
[50] Y. Liang, X. Zhang, Y. Liu, An efficient staggered grid material point method, Comput. Methods Appl. Mech. Engrg. 352 (2019) 85–109.
[51] V.P. Nguyen, A. de Vaucorbeil, C. Nguyen-Thanh, T.K. Mandal, A generalized particle in cell method for explicit solid dynamics, Comput. Methods Appl. Mech. Engrg. 371 (2020) 113308.
[52] A. de Vaucorbeil, V.P. Nguyen, C.R. Hutchinson, A total-Lagrangian material point method for solid mechanics problems involving large deformations, Comput. Methods Appl. Mech. Engrg. 360 (2020) 112783.
[53] J.-U. Song, H.-G. Kim, An improved material point method using moving least square shape functions, Comput. Part. Mech. 8 (2021) 751–766.
[54] L. Kan, Y. Liang, X. Zhang, A critical assessment and contact algorithm for the staggered grid material point method, Int. J. Mech. Mater. Des. 17 (4) (2021) 743–766.
[55] Q. Guo, X. Han, C. Fu, T. Gast, R. Tamstorf, J. Teran, A material point method for thin shells with frictional contact, ACM Trans. Graph. 37 (4) (2018) 1–15.
[56] J. Li, R. Ni, Z. Zeng, X. Zhang, An efficient solid shell material point method for large deformation of thin structures, Internat. J. Numer. Methods Engrg. 125 (1) (2024) e7359.
[57] P. Yang, Y. Liu, X. Zhang, X. Zhou, Y. Zhao, Simulation of fragmentation with material point method based on Gurson model and random failure, CMES - Comput. Model. Eng. Sci. 85 (3) (2012) 207.
[58] Z. Zhang, Y. Qiu, Z. Hu, H. Ye, H. Zhang, Y. Zheng, Explicit phase-field total Lagrangian material point method for the dynamic fracture of hyperelastic materials, Comput. Methods Appl. Mech. Engrg. 398 (2022) 115234.
[59] P. Hut, J. Makino, S. Mcmillan, Building a better leapfrog, Astrophys. J. 443 (2) (1995) L93–L96.
[60] S. Klinkel, F. Gruttmann, W. Wagner, A robust non-linear solid shell element based on a mixed variational formulation, Comput. Methods Appl. Mech. Engrg. 195 (1) (2006) 179–201.
[61] S. Seo, O. Min, J. Lee, Application of an improved contact algorithm for penetration analysis in SPH, Int. J. Impact Eng. 35 (6) (2008) 578–588.
[62] K. Ramajeyathilagam, C. Vendhan, Deformation and rupture of thin rectangular plates subjected to underwater shock, Int. J. Impact Eng. 30 (6) (2004) 699–719.
[63] R. Rajendran, K. Narasimhan, Damage prediction of clamped circular plates subjected to contact underwater explosion, Int. J. Impact Eng. 25 (4) (2001) 373–386.
[64] X. Zhu, Z. Zhang, R. Liu, Y. Zhu, Experimental study on the explosion resistance of cabin near shipboard of surface warship subjected to underwater contact explosion, Explos. Shock. Waves 24 (2) (2004) 133–139.